EXPERIMENTAL MODELLING OF THE DYNAMIC BEHAVIOUR OF A SPAR BUOY WIND TURBINE

*Giuseppe Roberto Tomasicchio [1], Felice D'Alessandro [1], Alberto Maria Avossa [2], Luigia Riefolo [2,3], Elena Musci [4], Francesco Ricciardelli [2], Diego Vicinanza [2,5]**

Abstract

This paper summarises the experience gained from wave basin experiments aimed at investigating the dynamic response of a spar buoy offshore wind turbine, under different wind and wave conditions. The tests were performed at the Danish Hydraulic Institute within the framework of the EU-Hydralab IV Integrated Infrastructure Initiative. The Froude-scaled model was subjected to regular and irregular waves, and to steady wind loads. Measurements were taken of hydrodynamics, displacements of the floating structure, wave induced forces at critical sections of the structure and at the mooring lines. First, free vibration tests were performed to obtain natural periods and damping ratios. Then, displacements, rotations, accelerations, and forces were measured under regular and irregular waves and three different wind conditions corresponding to cut-in, rated speed and cut-out. RAO, Statistical and spectral analyses were carried out to investigate the dynamic behaviour of the spar buoy wind turbine.

The results show that most of the dynamic response occurs at the wave frequency, with minor contributions at the first and second harmonics of this, and at the natural rigid-body frequencies. In addition, in many cases a non-negligible contribution was found at the first bending frequency of the structure; this suggests that Cauchy scaling of the model cannot be neglected.

According to the EU-Hydralab IV programme 'Rules and conditions' (www.hydralab.eu), the raw data are public domain, and therefore they represent a unique dataset of measurements, possibly useful for further analyses, for calibration and validation of numerical models, and for comparison with full scale observations.

Keywords: floating wind turbines; spar buoy; dynamic analyses; public datasets; hydrodynamic damping.

[1] Department of Engineering, University of Salento, Campus Ecotekne, via Monteroni, 73100 Lecce, Italy. e-mail: roberto.tomasicchio@unisalento.it; felice.dalessandro@unisalento.it

[2] Department of Engineering, University of Campania "Luigi Vanvitelli", via Roma 9, 81031 Aversa (CE), Italy. e-mail: albertomaria.avossa@unicampania.it; friccia@unicampania.it; diego.vicinanza@unicampania.it

[3] Department of Civil and Environmental Engineering, Politecnico di Milano, Piazza Leonardo da Vinci 32, 20133 Milan, Italy. e-mail: luigia.riefolo@polimi.it

[4] Autorità Idrica Pugliese Bari, Italy. e-mail: elena.musci@alice.it

[5] Stazione Zoologica Anton Dohrn, Villa Comunale, 80121 Napoli, Italy

**Corresponding author*

1. INTRODUCTION

In the last years, energy consumption has enormously increased worldwide. In this context, the European Union has set the goal of producing 22.1% of energy from renewable sources by 2020, in accordance with the Kyoto protocol. With the ambitious COP21 agreement, more nations will start down a path towards renewable energy production, as a pledge towards climate policies. Among the various energy sources, blue energy, holds a very promising and considerable potential in terms of wave, wind and tidal power [1-4]. This increased demand for renewable energy production has triggered a large amount of research on coastal and offshore devices, able to produce energy from waves, currents, and wind [5-10].

The vision for large scale offshore floating Wind Turbines (WTs) was introduced by Heronemus in 1972 [11], but it was not until the mid 1990s, after the commercial wind industry was well established, that the topic was taken up again by the mainstream research community [12]. While the fixed WT technology can be considered mature, and many turbines have been installed in water depths up to around 25 m, it is recognized that to reach the objectives of renewable energy production it will be necessary to expand the technology for deeper waters, adopting a floater as support structure for offshore WTs.

An offshore WT can use different floating system configurations. In fact, there is a large variety of floater geometries, of mooring systems and of ballast options used in the offshore oil and gas industry, which can be readily adapted by the wind energy industry. With particular reference to the platforms, they can be classified in terms of how they achieve stability in pitch and roll.

Currently, there are three main categories of offshore floating WT platform concepts: (a) the Tension Leg Platform (TLP), (b) the Spar buoy (SB) and (c) the Semi-Submersible (SS) platform (Figure 1). The TLP is made of a floating platform with lines tethered from its corners to concrete blocks or other mooring systems lying at the sea bottom. The SB is made of a long vertical floating cylinder having approximately half of its length underwater; the cylinder is ballasted in its lower part, which provides dynamic stability to the system. The SB is usually kept in position by a catenary spread mooring system using anchor-chains, steel cables and/or synthetic fibre ropes. The SS platform type comprises a few large column tubes connected to each other by tubular units; the column tubes contain the ballast and are partially filled with water. Stability is partly given by the ballast and partly by the width of the floater, giving and eccentricity to the buoyancy with respect to the centre of gravity; also the SS floater is kept in position by mooring lines.

Although the interest of the scientific community for floating offshore WTs is developing quickly, the dynamic behaviour of these structures under wave and wind actions remains an unsolved and complex issue, and a challenge in offshore engineering.

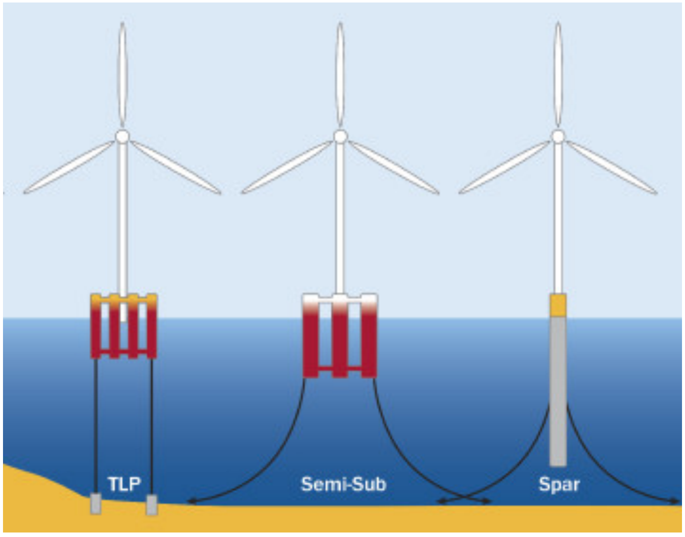

Figure 1. Spar buoy (SB), left, and tension leg platform (TLP), right, floating WTs.

Wave-structure interaction is bi-directional, i.e. the structure responds to the hydrodynamic loads and it in turns modifies the flow field around it. In particular, offshore structures are exposed to higher waves than coastal structures, as well as to a variety of different loading scenarios, among which short-crested wind waves in combination with strong winds, longer sea waves, gust bumps, broken waves, as well as and intense currents. Furthermore, slender cylindrical bodies are known to be subjected to vortex-induced motions. Laboratory experiments have shown the characteristics of the vortex shedding regime in the near field. Sumer and Fredsoe (2006) showed that flow separation induces drag and lift hydrodynamic forces which become prevalent to inertia forces [13]. Aristodemo et al. (2011) performed an extensive laboratory investigation in a vortex shedding regime of a smooth cylinder, and observed that an effect of the randomness of waves is a slight reduction of the inertia coefficient; this is associated with the quick changes in the vortex-flow regime [14]. Analysis and design of offshore WTs are made even more complicated by the presence of the rotor and by the action of the mooring lines [15]. Linear and higher-order diffraction and radiation forces, together with the nonlinear Morison’s type quadratic hydrodynamic drag loading imposed to the floating body, and with the nonlinear response of the mooring lines, gives rise to a highly complex coupled dynamic system. For the above reasons, evaluation of the design loads and expected dynamic response of offshore floating WTs becomes a tricky topic, involving coupled wave and wind models, and possibly considering a multivariate probability analysis aimed at pointing out extreme design conditions for combination of wave, wind, current and tidal events [16-18] and advanced load calculation methods [19-22].

The working features and, consequently, hydrodynamic response of floating offshore wind turbines needs being investigated through large-scale offshore engineering laboratory experiments. Previous experimental investigations allowed gaining information on flow characteristics and flow-induced forces for floating energy-conversion structures [23-27]. The recent interest in renewable energies has increased the demand of quality tests to optimize the design of innovative floating offshore wind turbines and to collect reliable and accurate data for further calibration and verification of numerical models [28]. Neverthless, there are still few studies on the SB concept, giving information concerning the flow characteristics around structures and the flow-induced forces, and experimental data on SB Floating Offshore Wind Turbines (FOWTs) are rarely published.

The first experiments of the Hywind SB wind turbine have been conducted at the Ocean Basin Laboratory at Marintek in Trondheim, where a 1:47 Froude-scaled model was investigated under a variety of sea states and wind velocities [29-31].

Then, Utsunomiya et al. [32], performed a 1:22.5 scale experiment using a SB platform in the offshore wave basin at National Maritime Research Institute (NMRI) in Tokyo, Japan. The SB is subjected to regular and irregular waves and to a steady horizontal wind force; then experimental results are compared with the numerical simulation results in order to validate the simulation method.

Subsequently, Myhr et al. [33] performed free decay, regular and irregular wave tests on a 1:100 scaled model of OC3-Hywind concept. They also checked the experimental results against those obtained from two numerical models using 3Dfloat and ANSYS, highlighting how physical model and numerical results agree reasonably well.

Again, a 1:128 scale model of OC3-Hywind was tested by Shin [34], under different meteocean conditions. The spar platform motions were captured and the RAOs (Response Amplitude Operator) were obtained.

Statoil's Hywind spar has also been tested at the Maritime Research Institute Netherlands (MARIN) with a 1:50 Froude-scaled model; then FAST offshore floating simulation tool was successfully calibrated and validated [35-37].

Sethuraman and Venugopal [38] tested a 1:100 scale wind turbine mounted on a stepped spar with four mooring lines, so to examine the hydrodynamic responses under regular and irregular waves and to calibrate a numerical model through OrcaFLex software. In particular, a good agreement with the experimental results was confirmed in terms of natural frequencies, wave surface elevation profiles and motion response at the centre of mass and nacelle.

Nallayarasu and Saravanapriya [39-40] studied the hydrodynamic behavior of a spar structure with taut and slack mooring in 250 m water depth, supporting 5MW turbine, using a 1:75 scaled model. The experiments with different mooring line angles of 0, 30 and 45 degrees at the seabed were conducted to obtain best mooring configuration under operating condition. An Ansys AQWA numerical model was also used to verify the data from the experiments. The influence of the turbine blade rotation on the motion response of the spar was investigated and the dynamic response under regular and random waves was examined. Comparison of measured response and simulated response for wind turbine rotation case showed reasonable match.

Recently, Ruzzo et al. [41] installed at sea a 1:30 scale model of the OC3-Hywind spar at the Natural Ocean Engineering Laboratory (NOEL) laboratory in Reggio Calabria (Italy), in order to investigate its behavior under real meteocean conditions.

Some preliminary outcomes of a comparison analyses between the experimental results on a 1:40 model of OC3-Hywind spar obtained in the DHI Offshore Wave Basin in Hørsholm (Denmark), and the corresponding response simulated through an aero-hydro-servo-elastic simulation FAST tool was presented by Tomasicchio et al. [42]. Finally, many studies of Floating Offshore Wind Turbines have been also conducted recently [43-47]. The dynamic behaviour of SB floaters has also been studied numerically [48-51].

The present paper describes some of the experience gained from physical model experiments aimed at investigating the dynamic response of SB FOWTs, and at overcoming the limitations in the available public domain dataset. In the test prototype SB and TPL were taken as reference, the MIT/NREL [15] and the OC3-Hywind [22, 36]. Different regular and irregular wave conditions were considered, together with three different wind intensities.

The objectives and the novelty of the research activity are: (a) exploring the feasibility of wave-basin experiments on FOWTs, and pointing out the major difficulties; (b) gaining basic knowledge of the hydrodynamic and dynamic behaviour of FOWTs; (c) investigating the interaction between the mooring lines and the floating body; (d) create a reliable database for numerical modelling calibration and verification; (e) create a reliable database for comparison with full scale measurements.

For the sake of brevity, the results presented in this paper are limited to the SB case. The TLP case will be considered separately. According to the EU-Hydralab IV programme ‘Rules and conditions’ (www.hydralab.eu), the raw data used for this paper are public domain.

The outcomes of the tests are examined through a time and frequency domain analysis of the displacements, rotations, accelerations and forces of the SB, to support the comparison of the results among the selected environmental conditions. Moreover, the results in terms of mooring line forces are presented. The remaining part of the paper is organized as follows. Details of experimental setup are reported in Section 2. Wave generation and basin instrumentation are discussed in Section 3. The test program is presented in Section 4. Results and the corresponding discussion are given in Section 5 for the regular and irregular wave tests, respectively. Finally, in Section 6 some conclusions are drawn.

2. SPAR BUOY PHYSICAL MODEL AND SETUP

The model was designed with reference to the OC3-Hywind prototype [44, 51]. This is a SB FOWT developed within the Offshore Code Comparison Collaboration (OC3), a project operating under Subtask 2 of the International Energy Agency (IEA) Wind Task 23.1. The OC3-Hywind system resembles the Hywind concept developed by Statoil Hydro in Norway; it features a 120 m, deeply drafted slender SB, with three catenaries mooring lines. The lines are attached to the platform by a delta connection (or “crowfoot”), to increase the yaw stiffness of the mooring system. The length scale of the Froude-scaled model is 1:40. Figure 2a shows a photo of the setup of the floating SB, while a sketch of the spar buoy model is represented in Figure 2b. Moreover, Tables 1, 2 and 3 summarize the geometric and dynamic properties of the prototype and model OC3-Hywind SB.

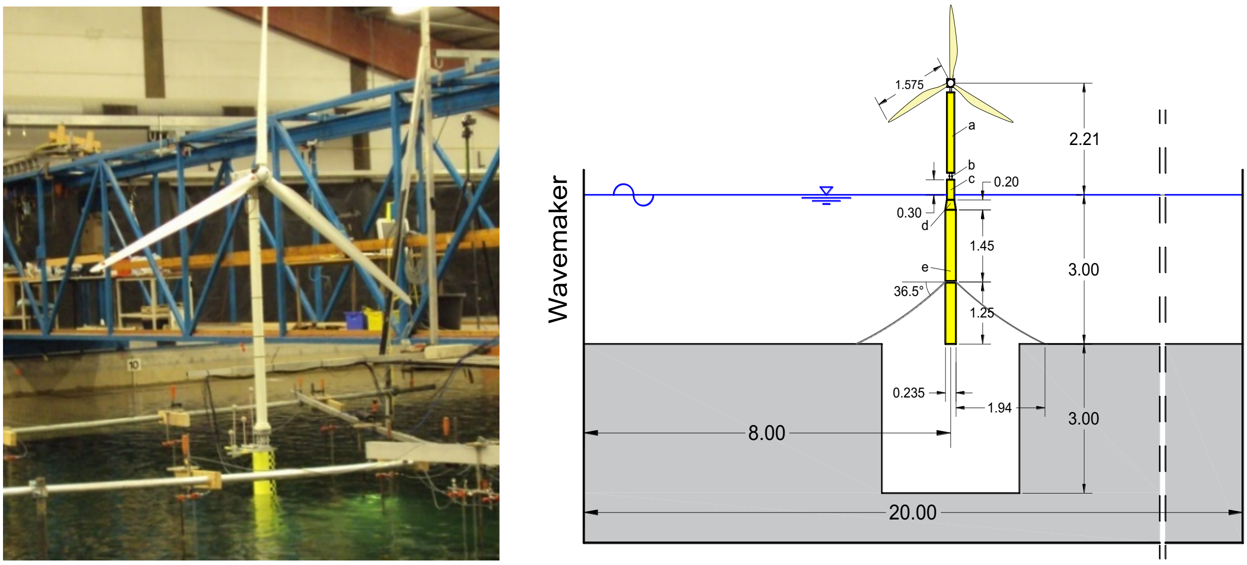

Figure 2. Spar buoy wind turbine model in the wave basin (left) and sketch (right) (depth/length in meters).

Table 1. Mooring coordinates in the scaled model.

Line	Fairleads			Anchors		
	x (m)	y (m)	z (m)	x (m)	y (m)	z (m)
1	0.118	0.000	-1.750	-1.950	0.000	-3.000
2	0.058	-0.100	-1.750	0.970	-1.675	-3.000
3	0.058	0.100	-1.750	0.970	1.675	-3.000

2.1 Floater characteristics

The floater of the SB model was designed consisting of five main parts (Figure 2), from top to bottom: (*a*) an upper cylinder, 1810 mm long with an outer diameter of 162.5 mm; (*b*) a 140 mm long connecting element for hosting load cells, (*c*) an intermediate cylinder, 400 mm long with an outer diameter of 162.5 mm, (*d*) a 200 mm long cone with an upper diameter of 162.5 mm and a lower diameter of 235 mm, and (*e*) a 2700 mm long cylinder with a diameter of 235 mm. The lower cylinder has a removable bottom 100 mm long, which was used to place the ballast. During the tests, the still water level (SWL) was 300 mm below the top of the intermediate cylinder. Ballast was designed to match scale requirements; lead bars and small lead spheres with a total weight of 92.5 kg were inserted at the bottom of the SB; a foam cover prevented the spheres from moving during testing.

Table 2. Geometric characteristics of the SB OC3-Hywind. Length scale λ = 1:40.

SB OC3-HYWIND	Full scale	Unit	Scale factor	Scaled model
SB diameter above taper	6.50	m	λ	0.162
SB diameter below taper	9.40	m	λ	0.235
Depth to top of taper below SWL	4.00	m	λ	0.100
Depth to bottom of taper below SWL	12	m	λ	0.300
Depth to floater base below SWL (total draft)	120	m	λ	3.000
Tower height	88.50	m	λ	2.212
Hub level	90	m	λ	2.250
Hub diameter	3.00	m	λ	0.075
Radius to fairleads	9.40	m	λ	0.235
Radius to anchors	9.40	m	λ	0.235
Depth to fairleads	70	m	λ	1.750
Depth to anchors	320	m	λ	8.000
Depth of C.o.M. below SWL	89.92	m	λ	2.248
Unstreached line length	902	m	λ	22.56
Line diameter	90	mm	λ	2.25
Angle between adjacent lines	120	Deg.	λ^0	120

Table 3. Dynamic properties of the SB OC3-Hywind. Length scale λ = 1:40.

SB OC3-HYWIND	Full scale	Unit	Scale factor	Scaled model
Rotor mass	110,000	kg	λ^3	1.677
Nacelle mass	240,000	kg	λ^3	3.658
Tower mass	347,500	kg	λ^3	5.297
Floating system mass (including ballast)	7,466,330	kg	λ^3	113.82
Total mass	8,163,830	kg	λ^3	124.45
Water displacement	8,029	m^3	λ^3	0.125
Buoyancy (water displacement x sea water density)	8,229,725	kg	λ^3	125.45
Buoyancy - Total Mass	65,895	kg	λ^3	1.004
Line mass density	78	kg/m	λ^2	0.0474
Suspended line = (Buoyancy – Total Mass) / (Line Mass density) / 3	283	m	λ	7.066

2.2 Mooring system design

According to Jonkman [44], the total vertical component of the force that the full-scale buoy experiences from the three mooring lines is 1,607 kN, therefore, each line applies a vertical force F_V = 535.7 kN to the SB. From the vertical component of the force, and considering that the submerged weight of the line per unit length is w = 698.1 N/m, it was possible to determine the length l_s of the suspended mooring line, assuming that this is inextensible:

$$l_s = \frac{F_V}{w} = 767.3\,\mathrm{m} \tag{1}$$

Being the vertical distance of the fairleads to the sea bottom D = 250 m, the horizontal component of the mooring force is [52]:

$$F_H = \frac{w(l_s^2 - D^2)}{2D} = 734.8\,\mathrm{kN} \tag{2}$$

The horizontal component of the suspended mooring line length is:

$$x = \frac{F_H}{w}\cosh^{-1}\left(\frac{wD}{F_H}+1\right) = 711.8\,\mathrm{m} \tag{3}$$

moreover, the distance x_A of the fairlead to the anchor is:

$$x_A = l - l_s + x = 846.7\,\mathrm{m} \tag{4}$$

l = 902.2 m being the total length of the line.

The design of the mooring system was carried out through a static analysis of one single line using STATMOOR Code [53]; this allows handling the static analysis of extensible mooring lines made of several segments, each of which having different geometric properties and with attached submerged buoys.

Inserting the value of F_H as input to STATMOOR, the static equilibrium configuration of a single mooring line was obtained, together with the vertical component of the force at the top and with the horizontal distance of the top of the line to the anchor. In Figure 3, the static shape of a mooring line is shown, corresponding to a horizontal force F_H, = 735 kN. This is very close to actual static equilibrium value for the mooring line, whereas for the largest selected horizontal force the whole mooring line is lifted from the sea bed. Consequently, the distance of the fairlead from the anchor at the equilibrium position is 847 m, with a length of chain lying on the seabed of approximately 134 m.

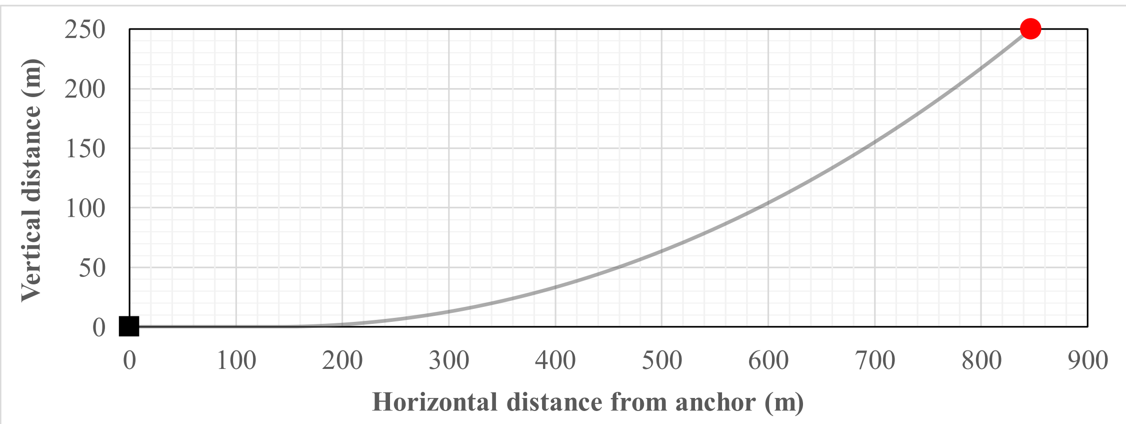

Figure 3. Static configuration of the single mooring (for F_H = 735 KN).

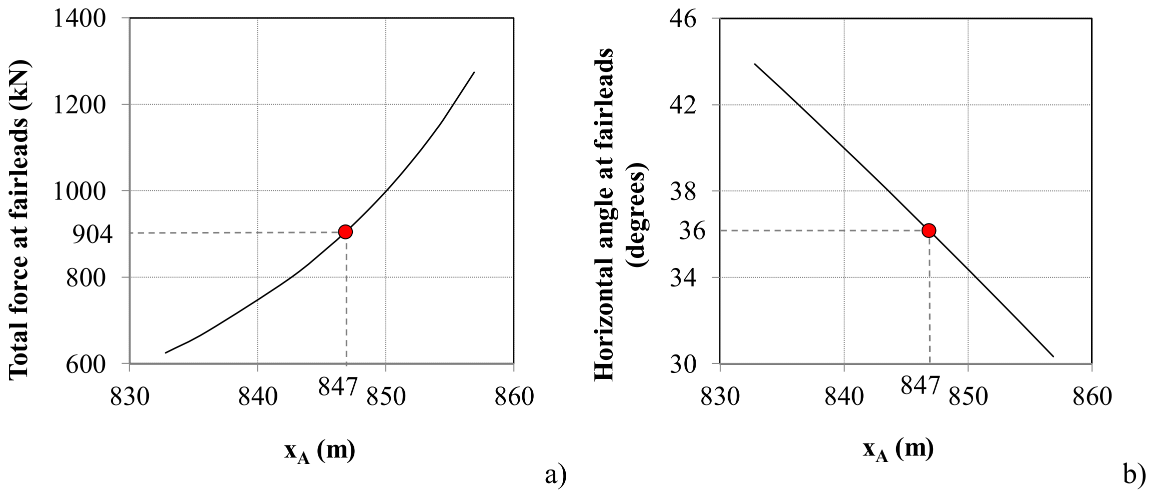

Figure 4. Total force at the mooring line's top from the anchor (a); angle at the mooring line's top with respect to the horizontal (b).

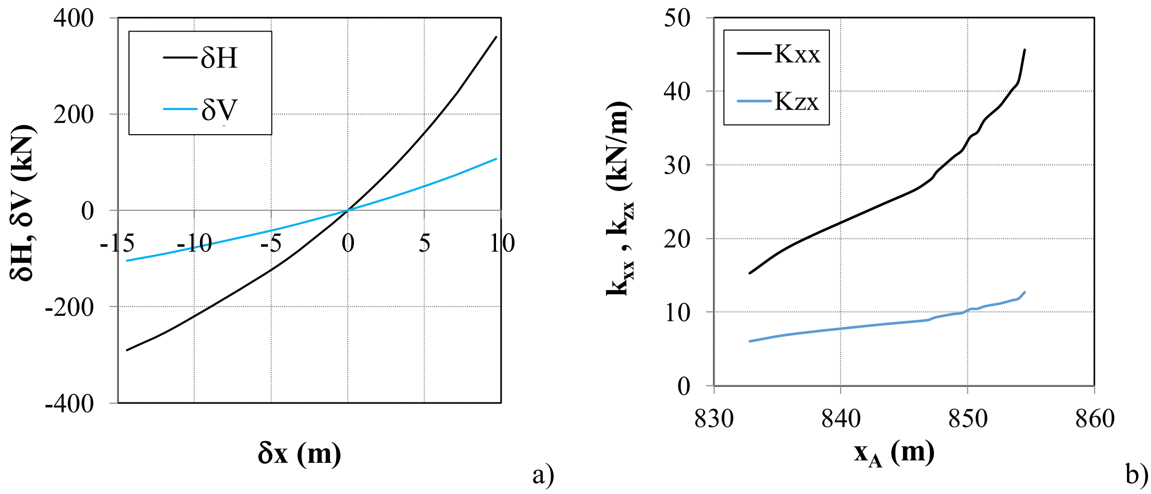

Figure 5. a) horizontal and vertical force increment at the fairleads due to an imposed lateral excursion (δ_x); b) horizontal (k_{xx}) and vertical (k_{zx}) stiffness for different distance of the fairleads to the anchor x_A.

In Figures 4a and 4b the total force at the upper mooring line's end and the corresponding angle with respect to the horizontal, is given as a function of its distance from the anchor. The lowest point in the first graph corresponds to the case of $F_H = 450$ kN, whereas the upper point corresponds to the position where the mooring line is completely lifted from the sea bed, and forms a zero angle with it. In Figure 5a the horizontal (δH) and vertical (δV) force increment at the line upper end due to an imposed horizontal displacement of the fairlead with respect to its initial equilibrium position, are shown. In Figure 5b the horizontal (k_H) and vertical (k_V) stiffness of the mooring line at the fairleads for different distance x_A to the anchor are also represented.

The OC3-Hywind prototype is located at 320 m water depth, whereas the 3 m deep basin allows reaching only a corresponding full-scale depth of 120 m in a scale of 1:40. As a consequence, considering that the fairleads were placed 1.75 m below SWL, the mooring lines were truncated at a vertical distance of 1.25 m and a horizontal distance of 1.94 m from the fairleads (Figure 2). The designed mooring system consisted of three lines directly connected to the main cylinder using a collar with fairleads; the angle between two adjacent mooring lines was 120°. Each line was made of a thin rope 1.7 mm in diameter, with a weight of 2.4 g/m and an axial stiffness of 6.25 N/mm. The mooring lines were pre-tensioned with weight of 14.7 N each, so to reproduce the same initial configuration in terms of zenithal angle (36°) and lateral force F_H at fairleads, and stiffness properties of the longer chain mooring lines. Force transducers having a maximum load capacity of 300 N measured the forces at the top of the three mooring lines. Between the transducers and the mooring lines, 0.75 m long springs were placed, with a stiffness of about 28.4 N/m.

2.3 Tower, rotor and blades

An overview of the instrumentation of the rotor and of the tower is given in Figures 6 and 7, respectively. Tables 4 and 5 summarize the properties of the WT and of the blades, respectively.

A six component force gauge was mounted at the base of the tower, between the tower and the floater, measuring $F_{x,base}$, $F_{y,base}$, $F_{z,base}$ and $M_{x,base}$, $M_{y,base}$ and $M_{z,base}$. The tower was made out of a plastic cylinder, with an outer diameter of 80 mm and a length of 1615 mm. At the top of the tower, between the tower and the nacelle, a four component force gauge was mounted, measuring $F_{x,top}$, $F_{y,top}$, $M_{x,top}$ and $M_{y,top}$. Furthermore, three accelerometers were placed at different levels along the tower; in particular, two accelerometers were located underneath the nacelle, measuring the lateral (y) and vertical (z) accelerations, and a third one at the bottom of the tower, measuring the longitudinal (x) acceleration.

(a) (b)

Figure 6. 6-DOF force gauges placed at the base of the tower (a). Rotor, nacelle and 4-DOF force gauge placed between the tower and the nacelle (b).

Table 4. Summary of properties of the WT. Length scale λ = 1:40.

WT	Full scale	Unit	Scale factor	Scaled model
Rotor mass	110,000	kg	λ^3	1.677
Nacelle mass	240,000	kg	λ^3	3.658
Rated rotor speed	12.1	rpm	λ^0	12.1
Overhang	5.00	m	λ	0.125
Shaft tilt	5.0	Deg.	λ^0	5.0

Table 5. Summary of properties of the blades.

Blade	Weight [g]	Centre of gravity [cm]
1	496	42.2
2	475	41.7
3	477	42.1

A motor inside the casing induced the rotation for the rotor. A potentiometer adjusted the rotational speed to 38 rpm, which corresponds to a rotational speed of 12.1 rpm full scale. This allowed for gyroscopic effects. The rotor blades were made of fiberglass and were geometrically scaled from a real case. Each blade had a length of 1.575 m (Figure 7). The pitch of the blades was set to 30°, giving rise to a measured thrust of 4 N at 38.1 rpm, model scale. Further tests to obtain a relationship between thrust and rotational speed were carried out with rotational speeds of 32 rpm and 42 rpm, model scale.

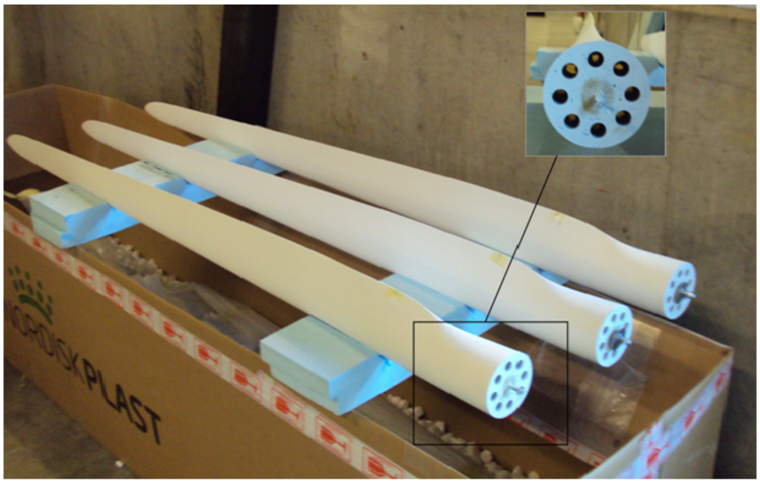

Figure 7. Blades profile and connection section.

Only static wind loads were reproduced, by applying the mean thrust force to the nacelle. This was done with a weightless line connected to the nacelle, passing through a pulley and with a suspended mass. The full-scale thrust for the 5 MW NREL reference turbine was calculated by different researchers, for example by Sclavounos *et al.* [54] who found that the rotor thrust under an 11 m/s wind is equal to about 800 kN, corresponding to 12.5 N for the 1:40 scaled model. Almost 4 N came from the trust force generated by the rotor, and the difference was obtained with a weight of 8 N.

3. WAVE GENERATION AND BASIN INSTRUMENTATION

The experiments were performed at the DHI Offshore Wave Basin in Hørsholm, Denmark. The wave basin (Figure 8) is 20 m long and 30 m wide, with a water depth of 3 m and a 6 m deep pit. The floating structure was placed at the centre of the pit, at a distance of 8 m from the wave maker, which lies on the 30 m wide side of the basin.

The wave maker is equipped with 60 individually controlled flaps, able of generating regular and irregular waves. A parabolic wave absorber located opposite to the wave maker minimized reflection. The characteristics of the incident and reflected waves were evaluated through a five wave-gauge array reflection analysis [55]. Wave calibration was made placing the five gauges at the centre of the pit; during the model tests, the gauges were moved 3 m downstream the floating structure. In addition, six wave gauges were located around the structure; an array of three was located 1.50 m upstream of the model and another array of three 1.50 m downstream the model.

A Nortek Vectrino velocimeter measured the velocity field in the proximity of the structure. The ADV was located at a distance of 60 cm from the front size of the floater. A Qualisys Track System (www.qualisys.com) tracked the six DoF rigid body motion of the model: surge, sway, heave, roll, pitch and yaw. The system is based on two cameras emitting infrared light. Five passive spherical markers, 40 mm in diameter, reflect the infrared light; these were positioned on a frame mounted at the tower base, just below the six-component force gauge. Data processed by the Qualisys Track Manager were directly transferred through an analog output to the main data acquisition system and thus synchronized with all other recorded data.

All the sensors were synchronized using the DHI Wave Synthesizer. Sampling took place at 40 Hz and lasted 3 minutes for each regular wave case and 10 minutes for each irregular wave case.

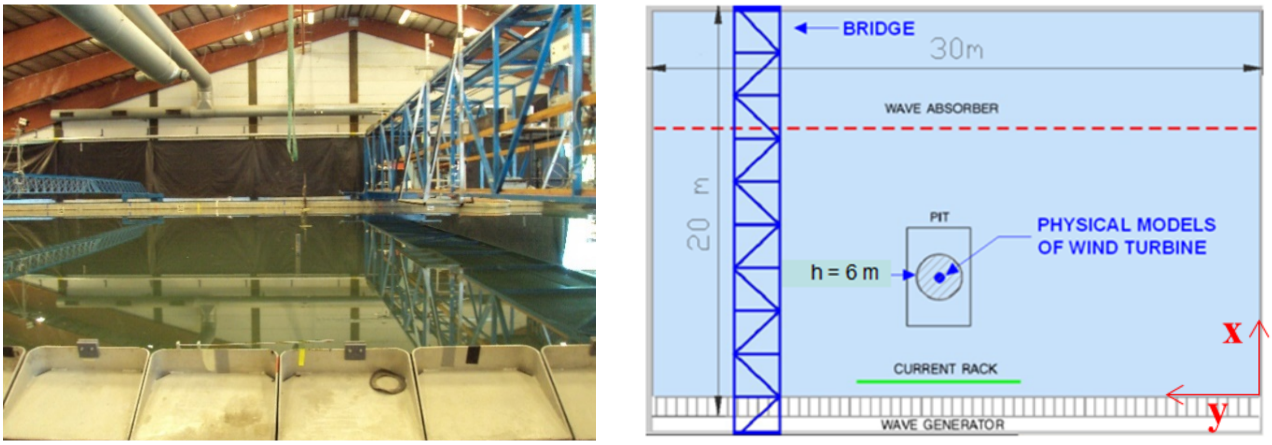

Figure 8. DHI Offshore Wave Basin in Hørsholm, Denmark.

4. TEST PROGRAM

According to IEC 61400-1 and IEC 61400-3 [56, 57], the three conditions of cut-in, of rated speed and cut-out were considered in the tests. First, cut-in conditions were tested; then, the rated speed condition was simulated, combining mean thrust, rotating rotor and different sea states with regular and irregular waves; finally, extreme wave conditions were generated, with the rotor being stopped and mean thrust corresponding to cut-out wind speed. Long-crested regular and irregular waves were generated, orthogonal (0°) and yawed (20°) to the structure. In Table 6 the characteristics of the generated waves are given, where H and T are the regular wave height and wave period, respectively, and H_s and T_p are the significant wave height and peak wave period, respectively.

Table 6. Test program.

Wind speed (rotor condition)	Waves	Prototype scale		Model scale	
		H or H_s [m]	T or T_p [s]	H or H_s [cm]	T or T_p [s]
0 m/s (parked) 11.4 m/s (rated)	Regular	1.00	10.1	2.5	1.6
		1.56	12.6	3.9	2.0
		1.80	15.2	4.5	2.4
		4	11.4	10	1.8
		6		15	
		8		20	
		6	12.6	15	2.0
			15.2		2.4
	Irregular	4	10.1	10	1.6
		6		15	
11.4 m/s (rated) 25 m/s (stalled)	Regular	10	11.4	25	1.8
		12	12.6	30	2.0
			15.2		2.4
	Irregular	8	12.6	20	2.0

5. RESULTS AND DISCUSSION

All data from the tests were converted to full scale using Froude scaling before being analysed. Only part of the data set is analysed in this manuscript. In particular, six tests with regular waves having the same height H and corresponding different period T, and different rotor conditions (parked/operational) were selected for RAO calculation (Table 7). Then, eight tests with different wave characteristics, H and T, and different rotor conditions (parked/operational) were here selected for frequency domain analyses (Table 8). Finally, two tests with the same irregular wave characteristics and same rotor conditions (parked/operational) were also selected for discussion (Table 9). For all the selected tests, wave incidence was orthogonal to the structure.

Table 7. Regular wave tests considered for RAO calculation.

H [m]	T [s]	Parked	Rated	Stalled
6	11.4	1381	1415	-
6	12.6	1383	1417	-
6	15.2	1384	1418	-

Table 8. Regular wave tests considered for frequency domain analyses.

H [m]	T [s]	Parked	Rated	Stalled
4	11.4	1380	1414	-
6	11.4	1381	1415	-
8	11.4	1382	1416	-
10	11.4	-	1481	1443

Table 9. Irregular wave tests considered in the analyses.

H **[m]**	***T*** **[s]**	**Parked**	**Rated**	**Stalled**
4	10.1	1385	1421	-

5.1 Free decay tests

Free decay tests were carried out to evaluate the surge, sway, roll and pitch natural frequencies and damping ratios of the SB wind turbine. Figure 9 shows the normalized Power Spectral Density Functions (PSDFs) $f \cdot S(f)/\sigma^2$ of the non-stationary measured surge, sway, pitch and roll, evaluated by MATLAB®. Natural frequencies of 0.011 Hz were found for the surge and sway motions and of 0.024 Hz for the roll and pitch motions (Table 10).

The power in a band of 0.01 Hz around the natural frequency was evaluated and found to be in the order of 99% of the total power for the surge, roll and pitch motions, and in the order of 97.5% for the sway motion (Table 10). Notice that there is a slight difference between the surge and sway frequencies, deriving from the different angles of the moorings for the two directions of movement; in the following we shall refer to a common surge/sway frequency of 0.011, and a common roll/pitch frequency of 0.024.

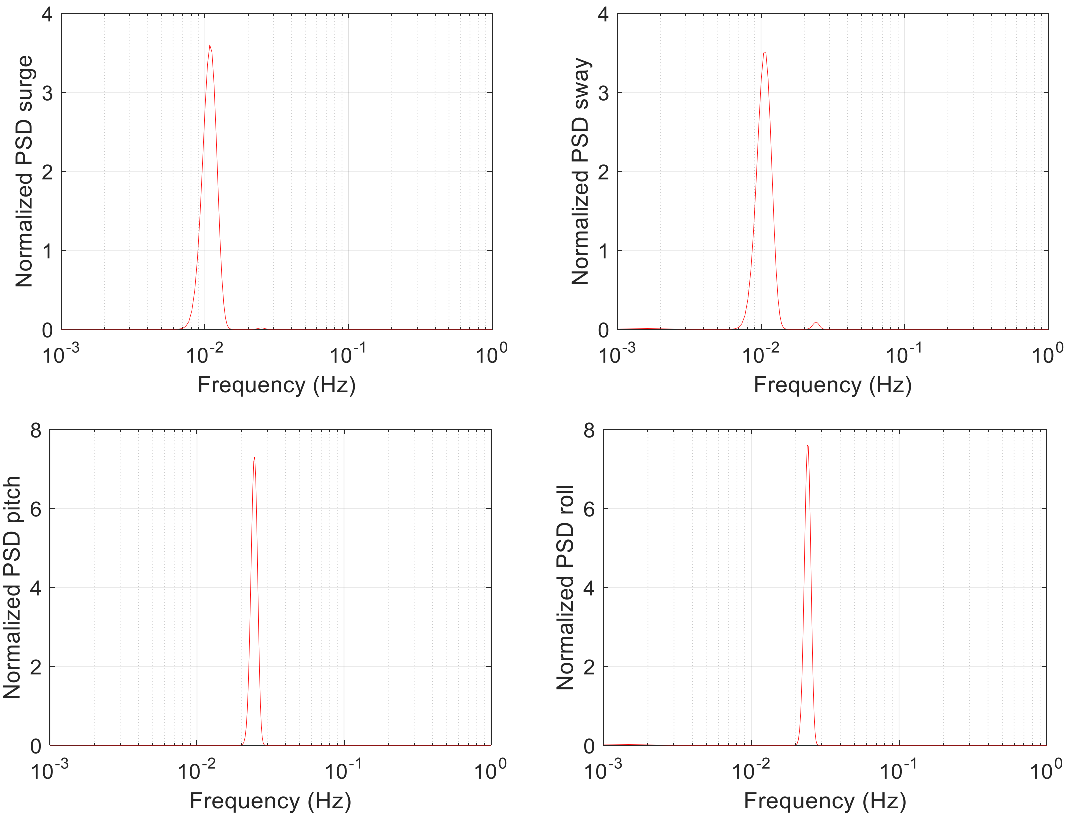

Figure 9. Normalized PSDFs from the free decay tests: surge and sway (top), pitch and roll (bottom).

Table 10. Natural periods and frequencies, band power and total power of surge, sway, roll and pitch motions.

D.o.F.	Period [s]	Frequency [Hz]	Band power		Total power	
Surge	88.5	0.0113	6.126	[m^2]	6.171	[m^2]
Sway	94.5	0.0106	23.97	[m^2]	24.58	[m^2]
Roll	41.5	0.0241	0.0220	[deg^2]	0.0221	[deg^2]
Pitch	40.9	0.0244	0.0096	[deg^2]	0.0097	[deg^2]

The damping ratio was calculated using the logarithmic decrement method, as a function of two response amplitudes X_j and X_{j+1} according to the following expression:

$$\xi = \frac{\delta}{\sqrt{4\pi^2 + \delta^2}} \tag{6}$$

where $\delta = (1/j)\ \ln(X_1/X_{j+1})$, j being the number of the cycles taken into account [58]. To quantify the non-linear nature of damping, the damping ratios were first calculated considering different numbers of cycles, as shown in Figure 10a. In this case, the strong nonlinearity of damping in the first cycle affects the average damping of the first seven cycles. The damping ratios were then calculated considering two consecutive peaks, therefore substituting X_j for X_1 in the evaluation of δ (Figure 10b). In particular, it is found that, besides the first cycle featuring a very large damping, the damping ratios stabilize at the second cycle, and become almost constant from the third cycle. In addition, damping appears to be only little dependent on Degrees of Freedom (D.o.F.); in particular values of 0.12, 0.19, 0.13 and 0.15 % were found for surge, sway, roll and pitch, respectively when the fourth cycle of oscillation was considered.

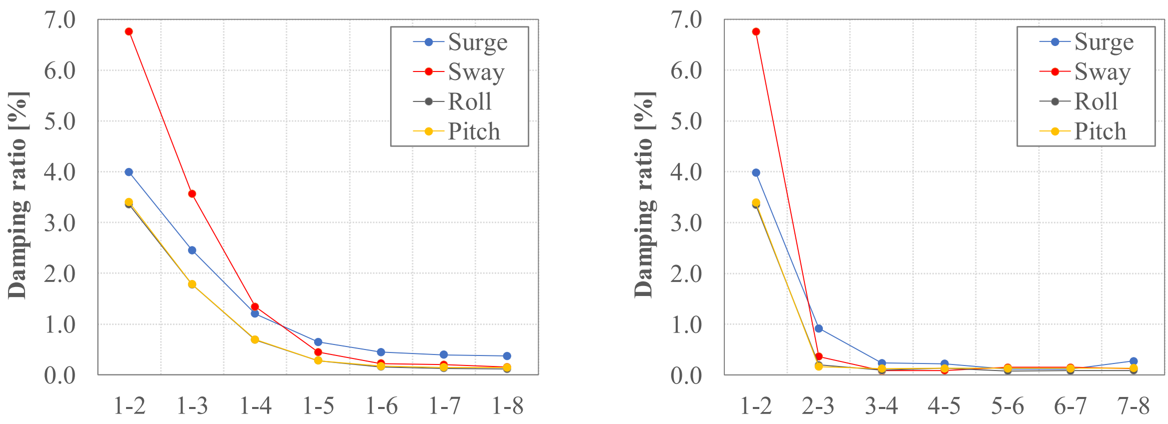

(a) (b)

Figure 10. Damping ratios for the surge, sway, roll and pitch motions from the free decay tests, obtained from the average logarithmic decrement considering the peaks X_1 and X_{j+1} (a) and two consecutive peaks (b).

5.2 Dynamic response to regular waves

5.2.1 Response Amplitude Operator and Frequency Domain Analysis results

In this section, the measured displacements, rotations, accelerations and forces at the top and base of the tower are discussed in the time and frequency domains, for the selected tests given in Tables 7 and 8. First, the results of motion responses for surge and pitch obtained from five regular waves are presented in the form of RAO. Sway and roll response is negligible being the heading angle of 0°, thus the related RAOs are not reported. Even though the number of tests to determine the RAO is not sufficient, few results are shown in Table 11. In particular, the surge and pitch RAO for large waves with H=6m is found to increase with increasing wave period. So, the surge and pitch responses grow steadily as the wave period increases. Moreover, an increase of surge and pitch RAO is observed in the operational condition if compared with parked conditions. These outcomes agree with the trends observed by Nallayarasu et al. [39] in experimental investigations on hydrodynamic response of spar-buoy wind turbine under regular waves.

Table 11. RAO for surge and pitch response.

rotor	H [m]	*T* [s]	Test N.	RAO surge [m/m]	RAO pitch [deg/m]
rated	6	11.4	1381	0.78	0.0185
	6	12.6	1383	0.98	0.0227
	6	15.2	1384	1.29	0.0264
parked	6	11.4	1415	0.87	0.0317
	6	12.6	1417	1.03	0.0367
	6	15.2	1418	1.32	0.0426

As an alternative, the dynamic response was calculated in terms of Power Spectral Density Function (PSDF). As an example, in figure 11 the PSDF of sway as measured in test #1382 is shown. The natural sway frequency of 0.011 Hz and the wave frequency of 0.088 Hz are clearly identified. In addition, the first two harmonics of the wave frequency are also visible at 0.176 Hz and 0.264 Hz; these are the effect of second-order hydrodynamic excitation, in agreement with Browing *et al*. [59]. Finally, a spike is also clearly visible at a frequency of 1.6 Hz. These five frequencies are recognized in almost all measured signals, with different relative amplitudes, depending on wave height, rotor condition, and measured quantity. The peak at 1.6 Hz is postulated to correspond to the first elastic bending frequency of the system. This was calculated to be 0.4 Hz or the prototype structure [59], and if Cauchy scaling were matched, it should have been the same on the model. Indeed, Cauchy scaling was not considered in the design of the model, therefore elastic frequencies are not accurately reproduced. This suggests that the measured signals be filtered in order to remove the frequencies at which elastic response occurs. In doing this one must be aware that if the elastic modes were properly reproduced in the model, these would have given a higher contribution to the total response than the one that is removed.

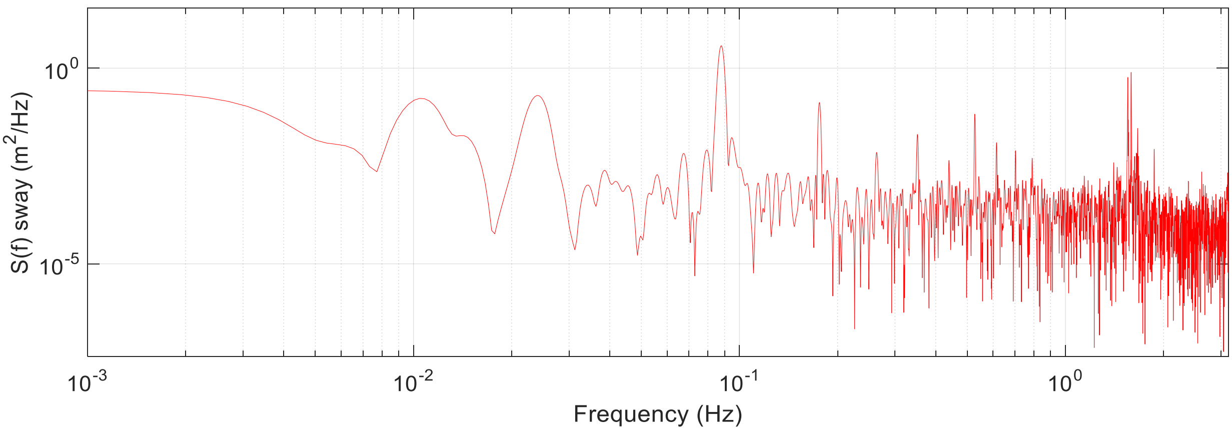

Figure 11. PSDF of sway as measured in test #1382.

Again for test #1382, in Figure 12 sample time histories of surge, sway, roll, pitch, $a_{x,base}$ and $a_{y,top}$ are shown. It is noted that all the quantities associated with a longitudinal motion are almost sinusoidal, with a frequency of 0.088 Hz, indicating that the motion takes place at the excitation frequency. The remaining quantities, which are associated with a lateral motion, show a quite different behaviour. Both sway and roll feature two different components, one at a frequency of 0.088 Hz, associated with the external excitation acting in the longitudinal direction, and the other at 0.83 Hz for sway and at 1.6 Hz for roll, the latter corresponding to the elastic frequency. For $a_{y,top}$ the response occurs mainly at 0.3 Hz.

The results discussed above where consistent among all the tests analysed, and this can be better seen from a frequency domain analysis.

In figure 13, the PSDFs of surge as measured in the eight tests listed in Table 8 are shown, together with a close-up view of the peaks at the first and second harmonic of the fundamental wave frequency. In all the tests the response is dominated by the wave frequency. It is noticed that in parked conditions the response increases with wave height at all frequencies of interest, whereas in operational conditions this trend is not always confirmed; this suggests that the gyroscopic effects and the rotor dynamics can somehow affect response.

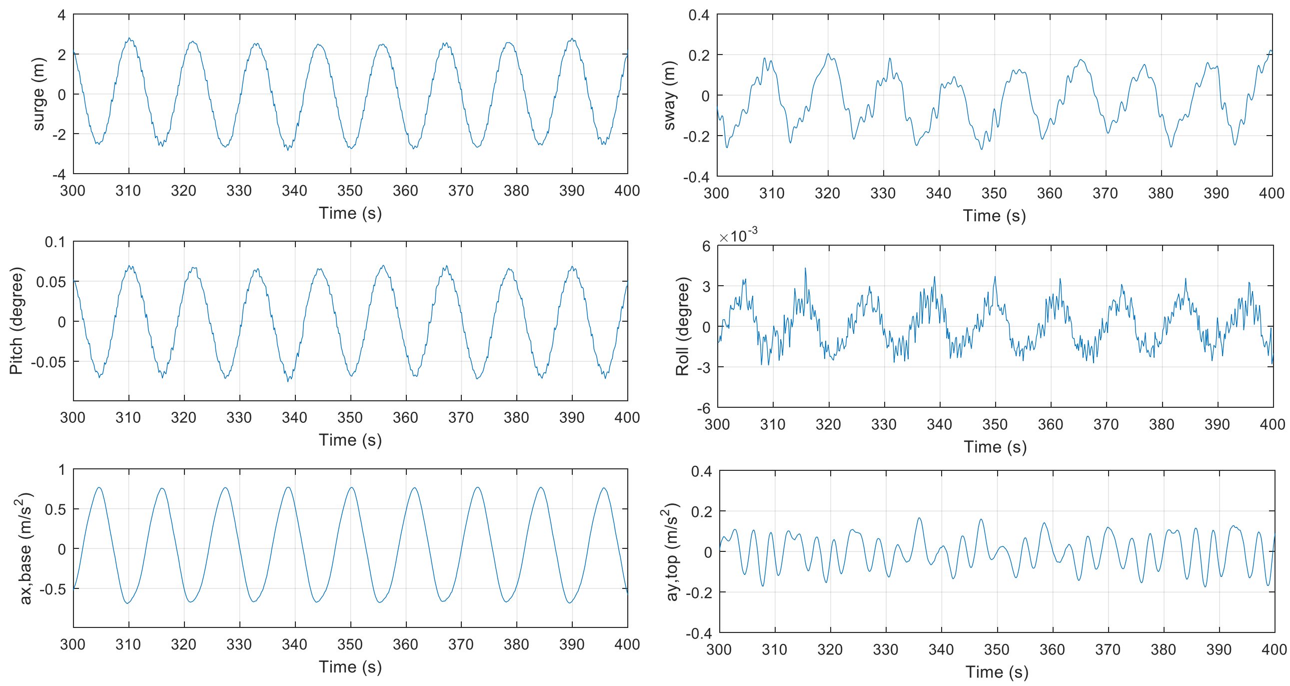

Figure 12. Sample time histories of surge, sway, roll, pitch, $a_{x,base}$ and $a_{y,top}$ as measured in test #1382.

Figure 14 shows, in the same format as Figure 13, the PSDFs of the longitudinal accelerations as measured in eight tests listed in Table 8, confirming the same results as those of Figure 13.

Figures 15 and 16 show the PSDFs of sway and of lateral accelerations as measured in eight tests listed in Table 8. For sway, the wave frequency is not dominant, but most of the excitation is at the oscillation frequency; on the other hand, for the accelerations higher frequency components are amplified and the wave frequency is dominant again.

To quantify the contribution of the different frequencies to the total response, Tables 12, 13 and 14 show the power corresponding to narrow ranges around the relevant frequencies, together with the total power, of the quantities associated with the lateral response. Only for sway in operational conditions, the fundamental wave frequency is not dominat, and contributes to the total response from 18.8% to 35.9%, whereas the oscillation frequency contributes to the total response from 15.1% to 49.1%; in this case there is also a contribution up to 32.9% at the roll frequency (not shown in the tables). For sway in parked conditions and for roll the wave frequency is dominant, with contributions to the total response from 78.4% to 87.8% for sway, and from 45.6%

to 98.9% for roll; the lowest contributions of the wave frequency to roll are accompained by contributions at its first harmonic, so that the sum of the two components is always greater than 84.5%. For the lateral acceleration the wave frequency and its harmonics (up to the third) contribute to the total response from 50.7% to 89.9%. The variability of the total variance of the longitudinal response parameters with oncoming wave height is parabolic, and common to all parameters, regardless of the rotor condition (parked or operational); for the lateral response parameters the variability with wave height is not as regular, and dependent on the particular parameter and on the turbine condition.

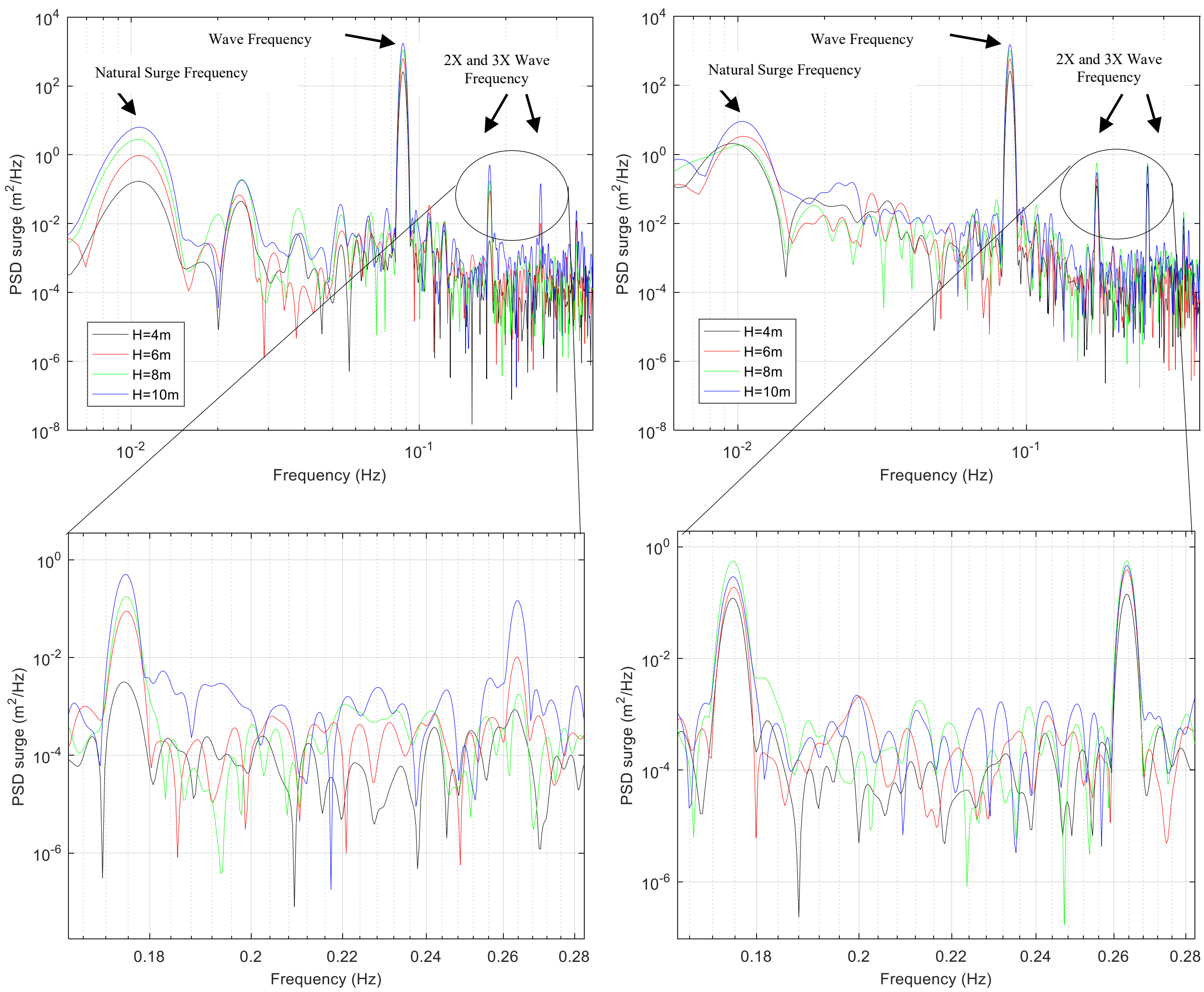

Figure 13. PSDFs of surge as measured in the different tests: parked conditions (left) and operational conditions (right). Close-up view of the peaks at the first and second harmonic of the wave frequency.

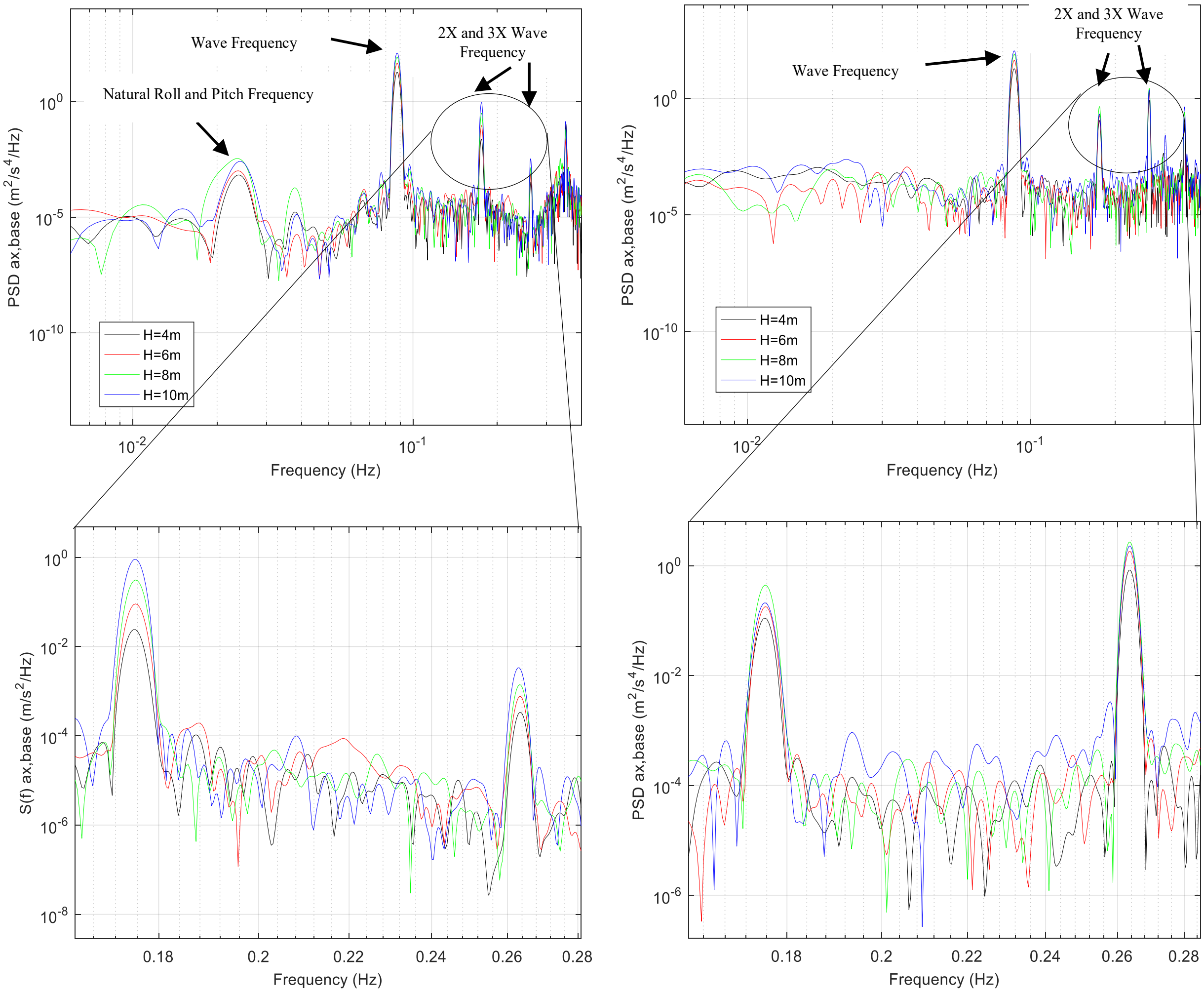

Figure 14. PSDFs of $a_{x,base}$ as measured in the different tests: parked conditions (left) and operational conditions (right). Close-up view of the peaks at the first and second harmonic of the wave frequency.

Similar calculations were carried out also for the quantities associated with the lateral response, which are not shown for the sake of brevity. Indeed, it is observed that in this case the fundamental wave frequency contributes to the total surge from 96.8% to 98.5%, to the total pitch from 97.1% to 99.1% and to the total longitudimal acceleration form 93.7% to 98.6%. Only in the case of the longitudinal acceleration there is a minor contribution of the second armonic of the wave frequency of up to 4.1%.

To validate the values of damping calculated from the free decay tests, damping ratios at the dominant vibration frequency were calculated from the PSDFs through the half-power bandwidth method. For the case of the surge response, the damping ratio evaluated in the different tests is compared with that calculated from free decay in figure 17; the results obtained in parked conditions are in quite good agreement with each other and with those coming from free decay. On the other hand, it is observed that for operational conditions there is a minor scatter of the measured damping ratio calculated in stationary conditions, and some difference with that calculated from free decay with stationary rotor; these differences are ascribed to gyroscopic effects. Furthermore, the operational wind turbine gives higher aerodynamic damping for surge motion and therefore lead to higher total damping. Such a behaviour is not confirmed by the extreme waves with H=10m. In fact, it is noted that for stalled condition (orange bar) the damping ratio is higher than for the operational condition. In this latter case the lower damping ratio is due to the gyroscopic effect.

Finally, in figure 18, the histograms of the occurrence frequencies of surge, sway, roll, pitch, $a_{x,base}$ and $a_{y,top}$ as evaluated from test #1382 are shown. Consistently with what previously observed, it is noticed that the quantities related to the longitudinal response feature a bimodal distribution, indicating an almost sinusoidal response. On the other hand, the histograms of the quantities related to the lateral response are rather different from the previous ones, and from one another; these appear to be associated with the combination of a narrowband process and a broader band process, whose relative intensity depends on the particular quantity observed.

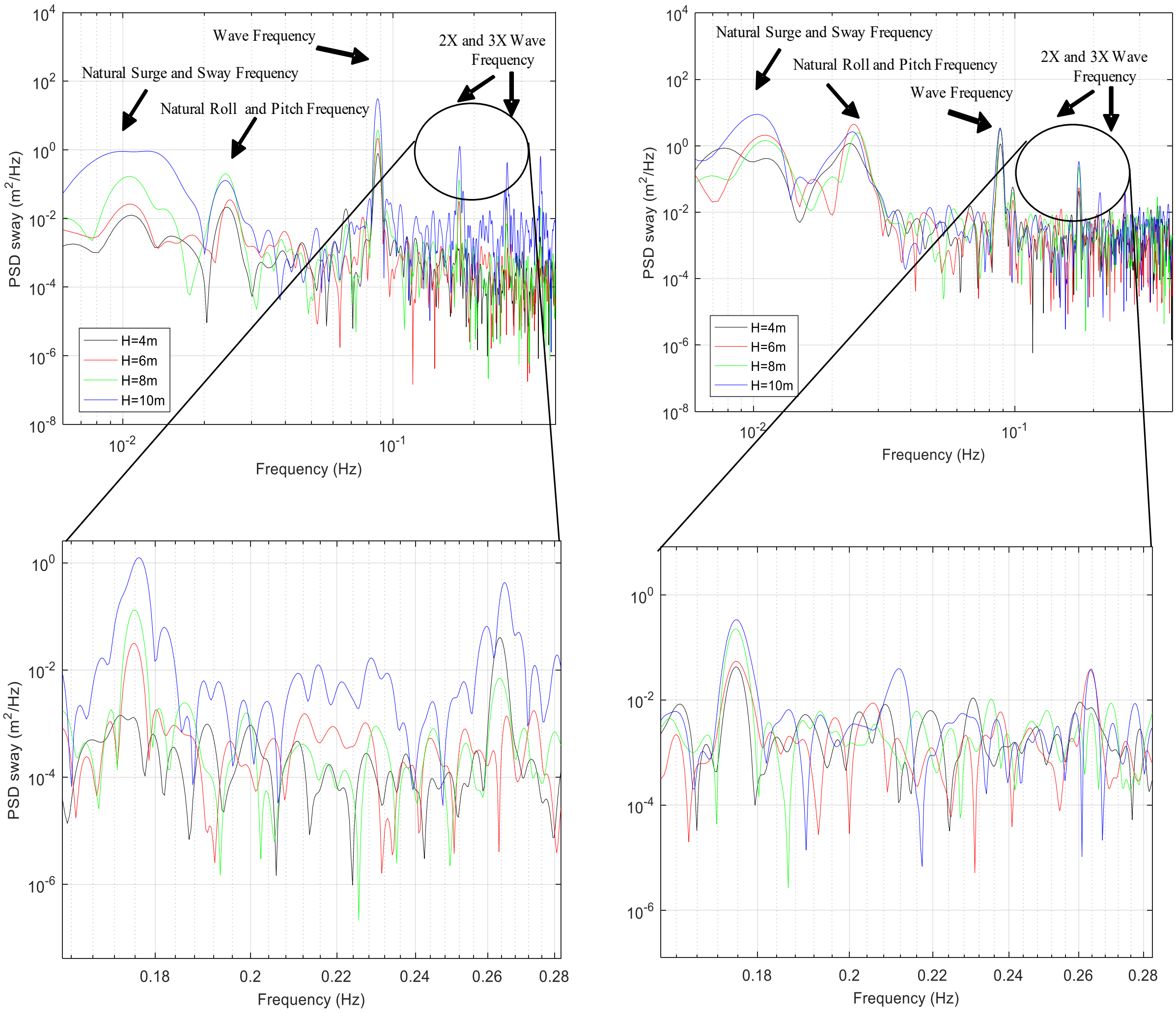

Figure 15. PSDFs of sway as measured in the different tests: parked conditions (left) and operational conditions (right). Close-up view of the peaks at the first and second harmonic of the wave frequency.

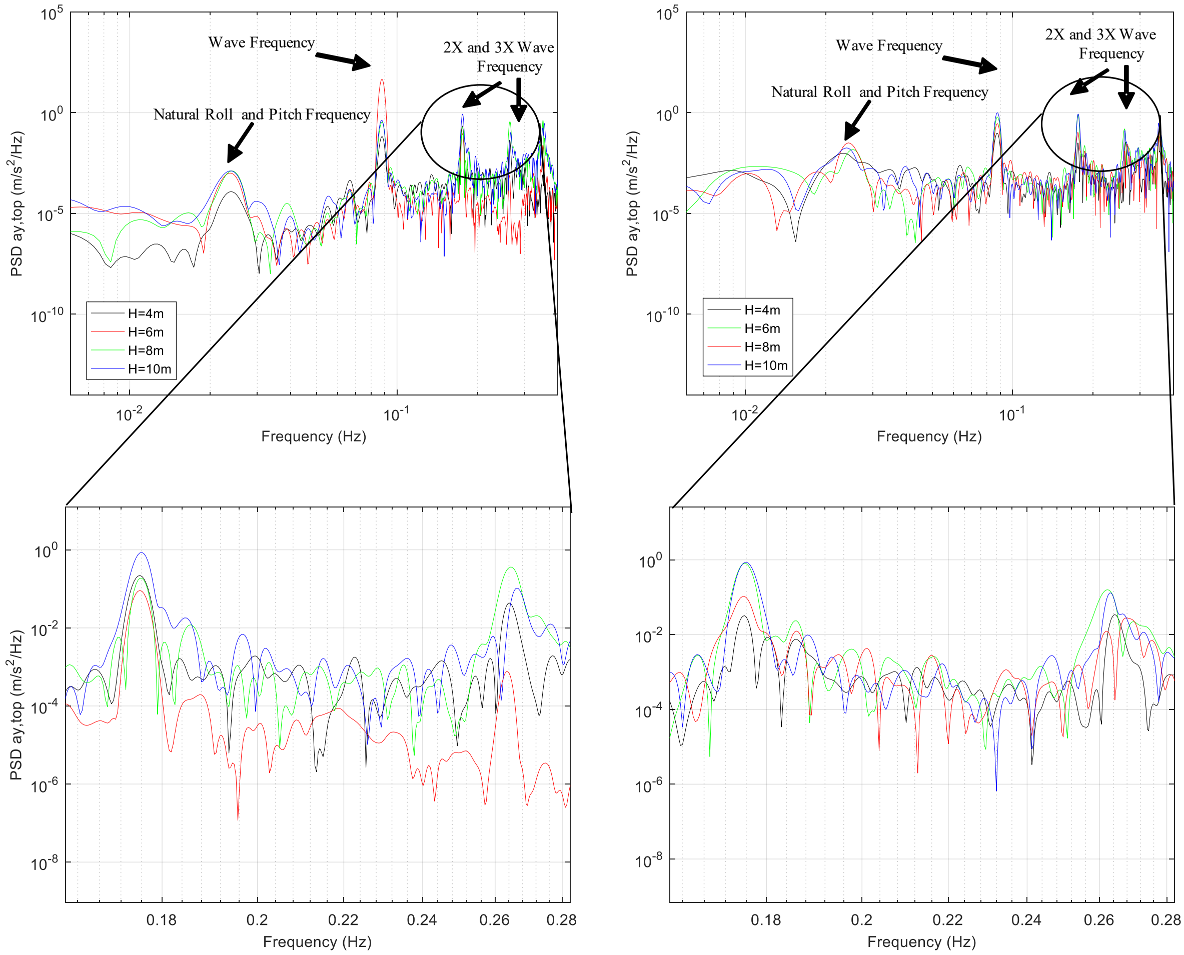

Figure 16. PSDFs of $a_{y,top}$ as measured in the different tests: parked conditions (left) and operational conditions (right). Close-up view of the peaks at the first and second harmonic of the wave frequency.

Table 12. Sway narrow-band and total power (m^2).

	Parked				Operational			
H (m)	4	6	8	10	4	6	8	10
Sway/Surge Frequency	3.44E-05	7.36E-05	4.62E-04	4.73E-03	3.47E-03	6.53E-03	4.38E-03	3.05E-02
Wave Frequency	2.51E-03	6.94E-03	1.18E-02	9.91E-02	3.53E-03	9.44E-03	9.94E-03	1.17E-02
2X Wave Frequency	8.33E-06	9.06E-05	3.77E-04	4.38E-03	1.32E-04	2.21E-04	7.33E-04	1.24E-03
3X Wave Frequency	1.30E-04	4.72E-06	2.09E-05	1.56E-03	6.28E-05	1.28E-04	4.08E-08	1.19E-04
Total power	3.20E-03	7.90E-03	1.50E-02	1.25E-01	1.19E-02	4.34E-02	2.77E-02	6.21E-02

Table 13. Roll narrow-band and total power (deg^2).

	Parked				Operational			
H (m)	4	6	8	10	4	6	8	10
Roll/Pitch Frequency	2.67E-09	4.66E-09	1.48E-08	8.37E-08	2.84E-07	3.38E-07	4.49E-07	4.20E-07
Wave Frequency	2.95E-07	9.01E-07	1.77E-06	3.78E-06	3.79E-06	1.10E-05	2.28E-05	3.27E-05
2X Wave Frequency	1.07E-07	2.96E-09	4.19E-08	3.22E-06	1.01E-07	6.59E-08	1.46E-07	7.78E-08
3X Wave Frequency	2.07E-08	2.05E-09	7.16E-09	1.20E-06	3.00E-08	1.21E-08	2.38E-08	1.99E-08
Total power	4.25E-07	9.11E-07	1.83E-06	8.28E-06	4.21E-06	1.14E-05	2.34E-05	3.32E-05

Table 14. Acceleration $a_{y,top}$ narrow-band and total power (m^2/s^4).

	Parked				Operational			
H (m)	4	6	8	10	4	6	8	10
Roll/Pitch Frequency	4.20E-07	1.08E-06	4.12E-06	4.88E-06	5.90E-05	1.02E-04	4.93E-05	7.49E-05
Wave Frequency	2.12E-04	5.23E-04	1.10E-03	1.39E-03	3.21E-04	8.91E-04	1.92E-03	3.17E-03
2X Wave Frequency	7.15E-04	5.96E-04	5.18E-04	2.79E-03	9.26E-05	4.02E-04	2.62E-03	2.97E-03
3X Wave Frequency	1.61E-04	6.83E-04	1.76E-04	2.80E-03	1.28E-04	1.41E-04	8.29E-04	5.22E-04
Total power	1.21E-03	2.79E-03	5.62E-03	7.35E-03	1.44E-03	2.87E-03	7.57E-03	1.02E-02

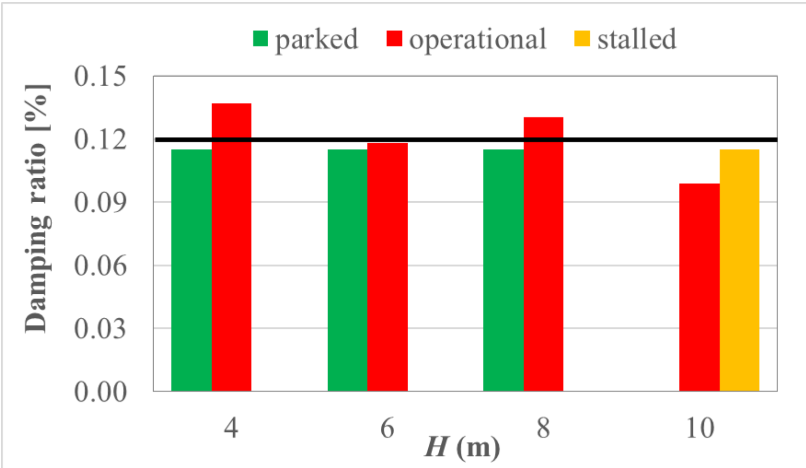

Figure 17. Damping ratios evaluated with the half-power bandwidth method in the surge D.o.F. for the different tests.

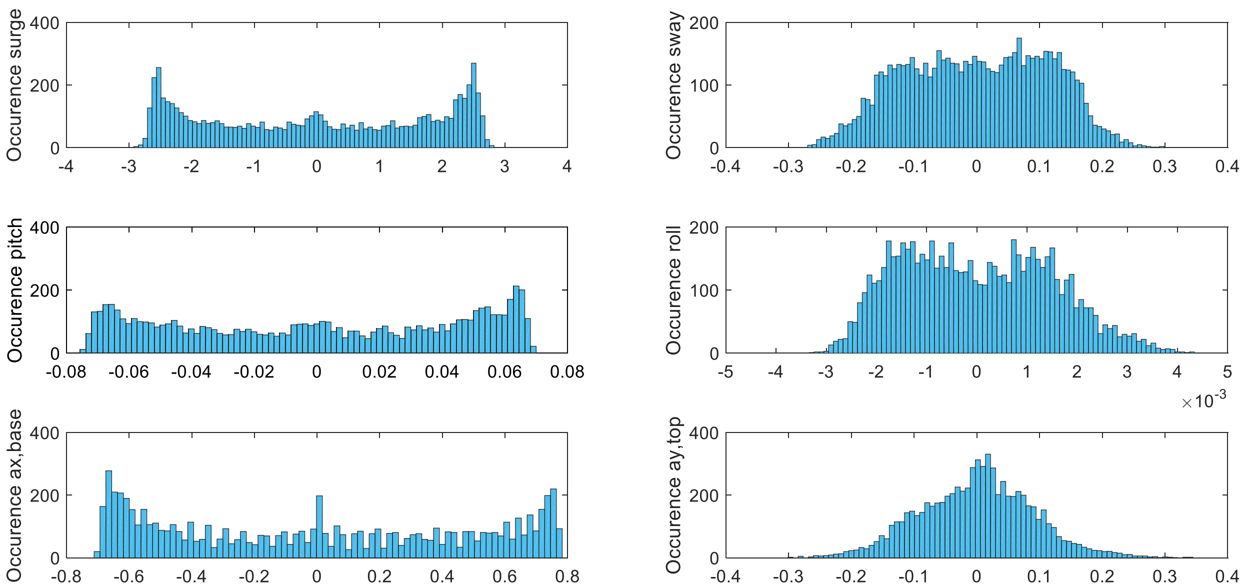

Figure 18. Histograms of the occurrence frequencies of surge, sway, roll, pitch, $a_{x,base}$ and $a_{y,top}$ as measured in test #1382.

5.2.2 Dynamic forces

Somehow similar conclusions to those presented for displacements and accelerations can be drawn for internal forces. In the same format as that of Tables 12 to 14, Tables 15 and 16 show the power corresponding to narrow ranges around the relevant frequencies, together with the total power of four of the lateral force components measured in the experiments. The wave frequency is always dominant, with contributions ranging from 50.4% to 84.8%; to the lowest components at the wave frequency, components at the first and second harmonics are associated, so that the sum is never lower than 74.4%. For the longitudinal force components similar calculations (tables are not shown) brought to values of 84.6% to 97.7% of the total force at the wave frequency.

Comparison between the measured displacements and corresponding forces is shown in figure 19. It is observed that RMS surge is a meaningful measure of the dynamic response, being the measured forces in general monotonically increasing with it. This happens in particular for the longitudinal forces, which are clearly associated with the longitudinal inertia; for the lateral forces no relation to the longitudinal inertia is expected, however, the trend is still reasonably good.

Table 15. Force $F_{y,base}$ narrow-band and total power (MN^2).

	parked				Operational			
H (m)	4	6	8	10	4	6	8	10
Roll/Pitch Frequency	2.29E-06	4.93E-06	2.62E-05	2.35E-05	3.79E-04	5.08E-04	2.75E-04	3.62E-04
Wave Frequency	1.57E-02	3.49E-02	5.75E-02	1.73E-01	1.35E-02	3.38E-02	5.67E-02	8.61E-02
2X Wave Frequency	2.41E-03	1.97E-03	8.66E-04	2.04E-02	6.76E-04	4.11E-03	2.31E-02	1.68E-02
3X Wave Frequency	6.65E-04	2.90E-03	3.90E-03	1.16E-03	1.62E-03	2.03E-03	3.30E-03	8.28E-04
Total power	1.87E-02	4.29E-02	7.09E-02	2.04E-01	1.90E-02	4.61E-02	9.13E-02	1.15E-01

Table 16. Force $F_{y,top}$ narrow-band and total power (MN^2).

	parked				Operational			
H (m)	4	6	8	10	4	6	8	10
Roll/Pitch Frequency	1.31E-06	2.12E-06	9.72E-06	9.57E-06	1.54E-04	2.07E-04	1.12E-04	1.52E-04
Wave Frequency	4.16E-03	9.17E-03	1.51E-02	1.67E-02	5.57E-03	1.68E-02	3.06E-02	4.30E-02
2X Wave Frequency	1.59E-03	1.26E-03	7.97E-04	7.14E-03	4.45E-04	1.53E-03	1.04E-02	9.04E-03
3X Wave Frequency	4.48E-04	1.82E-03	3.45E-03	1.43E-03	4.07E-04	5.82E-04	1.55E-06	8.22E-04
Total power	6.63E-03	1.48E-02	2.60E-02	3.31E-02	9.52E-03	2.39E-02	4.92E-02	6.20E-02

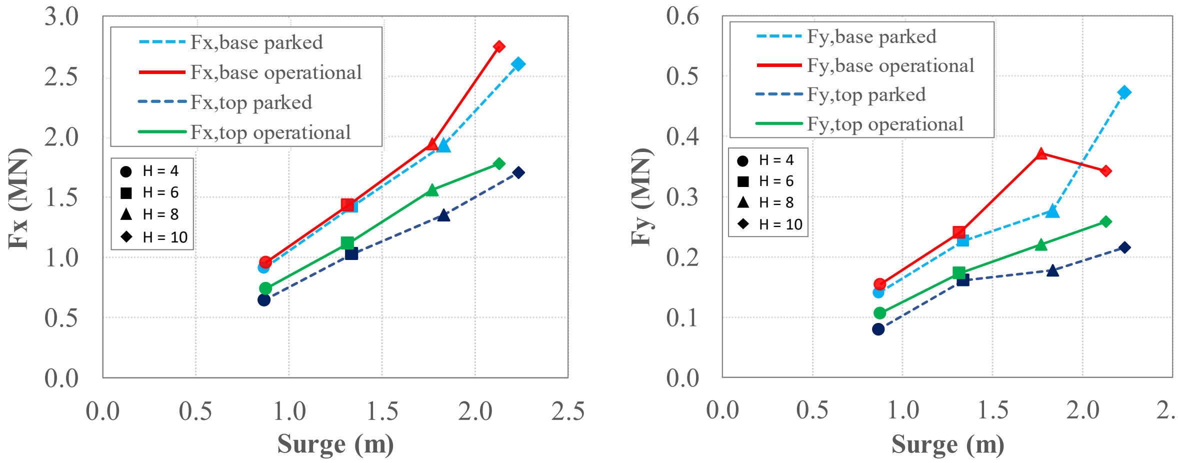

(a) (b)

Figure 19. STD of the measured force as a function of the STD of surge in (*a*) longitudinal and (*b*) transverse directions.

5.2.3 Peak factors and expected maxima

The experimental results presented can be used to evaluate the expected maxima of the response parameters. In Table 17 the STD of the ten discussed response parameters (displacements, rotations, accelerations and forces) are summarised for the eight tests.

To the aim of obtaining expected response peak values, the peak factors were determined according to Vanmarcke [60, 61].

Table 17. STD of displacements, rotations, accelerations and forces.

	parked				operational			
H (m)	4	6	8	10	4	6	8	10
Surge (m)	0.8672	1.340	1.833	2.234	0.8758	1.317	1.770	2.130
Sway (m)	0.0566	0.0889	0.1072	0.3536	0.1091	0.2083	0.1664	0.2492
Pitch (deg)	0.0204	0.0330	0.0458	0.0576	0.0199	0.0362	0.0407	0.0759
Roll (deg)	0.0007	0.0010	0.0014	0.0040	0.0023	0.0036	0.0050	0.0059
$a_{x,base}$ (m/s^2)	0.2330	0.3617	0.4893	0.6099	0.2396	0.3608	0.4821	0.5740
$a_{y,top}$ (m/s^2)	0.0348	0.0529	0.0750	0.0857	0.0380	0.0536	0.0870	0.1012
$F_{x,\mathrm{base}}$ (MN)	0.9086	1.420	1.933	2.598	0.9566	1.427	1.938	2.748
$F_{y,\mathrm{base}}$ (MN)	0.1402	0.2071	0.2663	0.4521	0.1378	0.2148	0.3022	0.3392
$F_{x,\mathrm{top}}$ (MN)	0.6426	1.024	1.352	1.702	0.7396	1.112	1.560	1.776
$F_{y,\mathrm{top}}$ (MN)	0.0815	0.1218	0.1611	0.1818	0.0959	0.1547	0.2219	0.2483

The spectral moments were computed by numerical integration. The peak factors for surge, pitch and longitudinal acceleration and forces have been calculated based on the bimodal PSD method; the concept of bimodal PSD can be generalized including all the structural responses with two dominant frequency ranges [62]. The overall dynamic process has been analysed applying two different approaches for the different spectral bands, to define a combined peak factor. In particular, the first approach considers the spectral band around the wave frequency as a very narrow band process. Thus, the corresponding peak factor g_{x1} of a sinusoidal process, equal to $\sqrt{2}$ was assumed. The second approach was applied to the remaining, higher frequency range, as a Gaussian process. Accordingly, the Vanmarcke approach was applied to calculate the corresponding peak factor g_{x2}. Finally, to evaluate the overal maximun response, the Square Root of the Sum of the Squares (SRSS) rule was used to combine the two peak response components [63] as follow:

$$Max\,value = \sqrt{g_{x1}^2\,\sigma_{x1}^2 + g_{x2}^2\,\sigma_{x2}^2} \tag{7}$$

where σ_{x1}^2 and σ_{x2}^2 are the variance of the two frequency components of the process, calculated from the corresponding spectral moment.

The peak factors for sway, roll and lateral acceleration and forces were calculated based only on the approach proposed by Vanmarcke, applying to Gaussian, narrowband processes.

The peak factors calculated as above, over a duration of 1,053 seconds, that represent the duration of the tests, are summarized in Table 18, together with the measured peak factors (in brackets, max/STD) over the same record.

It is observed that the prediction of the peak factor of the longitudinal components of the response is quite accurate, with average errors in the order of 9% in parked conditions and 11% in operational conditions. This indicates that the bimodal method performs well in this case. On the other hand, the prediction of the peak factor of the lateral components of the response is much more scattered and less accurate, with errors ranging from 2% to 100%. This is due to the fact that some of the lateral components of the response are nearly Gaussian (e.g. $a_{y,top}$), in which case the prediction is fairly accurate; in some others they are quite away from being Gaussian (e.g. $F_{y,base}$), and the prediction becomes poor.

Table 18. Calculated (measured) peak factors of displacements, rotations, accelerations and forces.

	Parked				Operational			
H (m)	4	6	8	10	4	6	8	10
Surge	1.44 (1.49)	1.43 (1.52)	1.43 (1.53)	1.43 (1.55)	1.46 (1.83)	1.44 (1.64)	1.43 (1.66)	1.43 (1.74)
Sway	3.54 (2.43)	3.47 (2.25)	3.51 (2.65)	3.57 (2.92)	3.60 (3.56)	3.40 (3.83)	3.52 (4.13)	3.42 (3.21)
Pitch	1.47 (1.43)	1.44 (1.49)	1.44 (1.47)	1.52 (1.70)	1.54 (1.82)	1.47 (1.80)	1.46 (1.71)	1.46 (1.71)
Roll	3.60 (2.60)	3.55 (2.11)	3.57 (2.64)	3.73 (3.00)	3.56 (3.23)	3.45 (2.15)	3.43 (1.99)	3.41 (1.88)
$a_{x,base}$	1.45 (1.58)	1.43 (1.56)	1.43 (1.60)	1.45 (1.72)	1.64 (1.68)	1.60 (1.71)	1.58 (1.80)	1.52 (1.77)
$a_{y,top}$	3.45 (2.73)	3.57 (3.40)	3.58 (3.80)	3.57 (4.86)	3.75 (3.25)	3.70 (3.64)	3.63 (3.23)	3.62 (3.55)
$F_{x,\mathrm{base}}$	1.47 (1.65)	1.45 (1.68)	1.47 (1.69)	1.49 (1.67)	1.67 (1.47)	1.62 (1.53)	1.74 (1.59)	1.55 (1.49)
$F_{y,\mathrm{base}}$	3.37 (1.66)	3.43 (2.29)	3.47 (2.67)	3.38 (2.56)	3.45 (2.78)	3.45 (1.92)	3.44 (2.39)	3.45 (2.56)
$F_{x,\mathrm{top}}$	1.50 (1.71)	1.45 (1.75)	1.49 (1.74)	1.53 (1.71)	1.90 (1.84)	1.84 (1.66)	1.91 (1.61)	1.66 (1.70)
$F_{y,\mathrm{top}}$	3.43 (2.09)	3.52 (2.96)	3.56 (3.13)	3.54 (2.74)	3.57 (3.18)	3.53 (2.49)	3.49 (2.93)	3.49 (2.74)

5.2.4 Mooring lines forces

Analysis of the mooring line forces revealed a strong sensitivity of the measured data on the alignment of the lines with the oncoming waves. In the experimental setup mooring line 1 was aligned with the oncoming waves and the mooring lines 2 and 3 were symmetric at an angle of 120° with mooring line 1. The analysis of measured forces indicated an asymmetric behaviour, which was ascribed to a no perfect alignment in the setup. In Figure 20a a sample time history of the force measured in test #1380 is shown, clearly indicated the non-symmetric behaviour. Therefore, a correction was applied to the force components, minimizing the difference between the measured mean force in lines 2 and 3. This procedure indicated a misalignment of the experimental setup of 3.63° with respect to the oncoming wave direction. In figure 20b the corrected sample time histories for test #1380 are shown; in the corrected time histories line 1 is aligned with the oncoming wave direction, but a slight asymmetry between lines 2 and 3 is still present, indicating a discrepancy between the actual angles between line 1 and lines 2 and 3, and the theoretical value of 120°. This latter experimental error cannot be corrected with post processing. In Figure 21 the PSDFs of the mooring line 1 tension for the parked and operational conditions are shown. Like displacement and acceleration spectra, shown in figures 13 to 16, the surge, sway, pitch and roll oscillations frequencies are clearly visible, together with the oncoming wave frequency and first and second harmonics; in addition, the heave natural oscillation frequency is also visible at 0.034 Hz. Heave response appears to be more than linearly increasing with wave height. Table 19 shows the power corresponding to narrow ranges around the relevant frequencies, together with the total power of the force in mooring line 1. In this case, almost all the energy is concentrated at the wave frequency, from 97.3% to 99.2% of the total power.

Globally, it is observed that the dynamic forces in the mooring lines are larger in parked conditions than in operational conditions, essentially due to the different dynamic response of the system coming from the presence of aerodynamic damping.

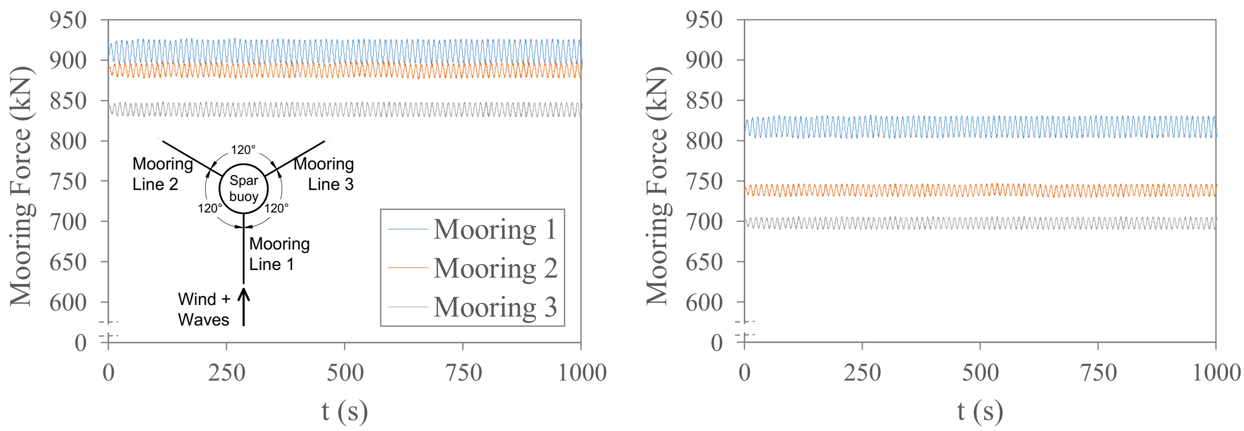

(a) (b)

Figure 20. Sample time histories of mooring line forces for test #1380: raw data (a), corrected data (b).

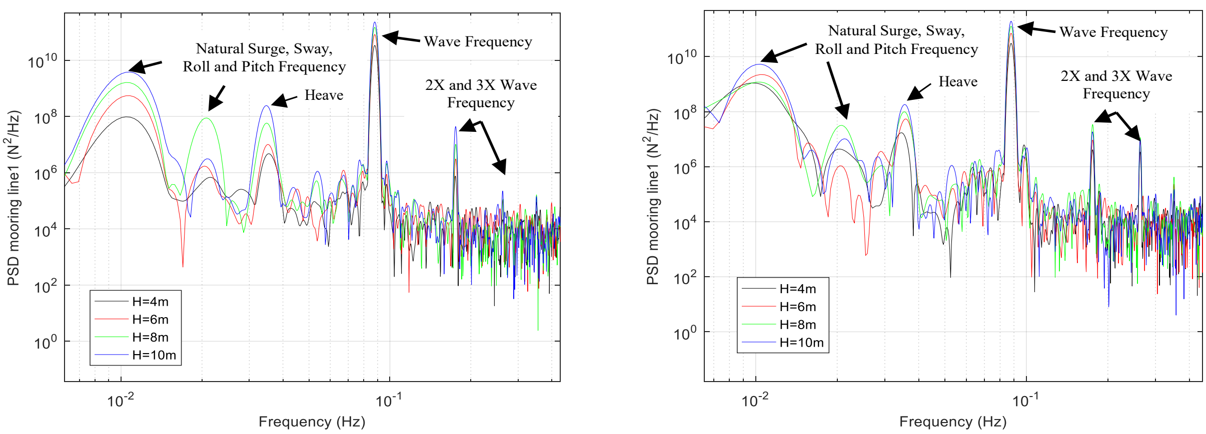

Figure 21. PSDFs of forces in mooring line 1 for parked (left) and operational (right) conditions.

In Figure 22 a sample time history and the histogram of the occurrence frequencies of the force in mooring line 1 as measured in test #1380, are shown. As expected, it appears that the process is almost sinusoidal, with a minor component at a higher frequency. This suggests that the bimodal method is used for evaluating the peak factors. In Table 20 the mean, STD and calculated and measured peak factors of the force in mooring line 1, are given. Also, in this case the dynamic forces are proportional to the oncoming wave height, whereas the mean forces are very little affected by it. Comparison between the calculated and measured values of the peak factors indicate that calculated values are almost coincident with the value of $\sqrt{2}$ applying to a sinusoidal process, whereas the measured value is some 13% larger, indicating the presence of higher frequency component.

Table 19. Mooring line 1 force narrowband and total power (N^2).

	Parked				Operational			
H (m)	4	6	8	10	4	6	8	10
Surge/Sway Frequency	2.13E+05	1.47E+06	4.01E+06	9.61E+06	1.83E+06	4.66E+06	3.24E+06	1.08E+07
Pitch/Roll Frequency	9.13E+02	3.63E+03	1.56E+05	1.12E+04	1.74E+04	8.94E+03	5.77E+04	4.37E+04
Heave Frequency	7.72E+03	2.08E+04	8.61E+04	5.33E+05	2.96E+04	7.22E+04	1.84E+05	3.49E+05
Wave Frequency	1.02E+08	2.50E+08	4.49E+08	6.95E+08	9.34E+07	2.17E+08	3.90E+08	5.86E+08
2X Wave Frequency	2.95E+03	9.89E+03	3.31E+04	1.32E+05	1.52E+04	3.16E+04	1.16E+05	5.03E+04
3X Wave Frequency	2.92E+02	5.29E+02	3.31E+04	1.47E+03	1.07E+04	2.51E+04	3.32E+04	2.75E+04
Total power	1.03E+08	2.52E+08	4.54E+08	7.06E+08	9.60E+07	2.23E+08	3.95E+08	5.99E+08

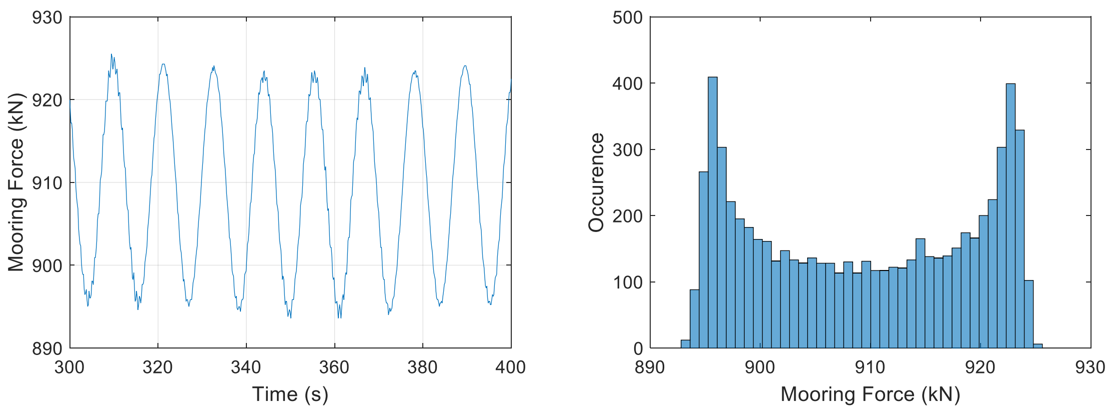

Figure 22. Sample time history and histogram of the occurrence frequencies of the force in mooring line 1 as measured in test #1380.

Table 20. Mean, STD and calculated (measured) peak factor of the force in mooring line 1.

	Parked				Operational			
H (m)	4	6	8	10	4	6	8	10
Mean [kN]	909.3	909.9	911.0	924.3	1249.6	1254.4	1263.0	1246.9
STD [kN]	10.13	15.85	21.30	26.56	9.76	14.88	19.81	24.42
Peak factor	1.42 (1.64)	1.42 (1.64)	1.42 (1.69)	1.42 (1.55)	1.43 (1.63)	1.42 (1.63)	1.42 (1.67)	1.42 (1.63)

5.3 Dynamic response to irregular waves

5.3.1 Response Amplitude Operator and Spectral Analysis results

In the present section the RAO and PSD diagrams corresponding to two selected irregular tests under parked and rated conditions (Table 9) are presented. For irregular waves the calculation of RAO is carried out in frequency domain. In fact, it is possible to find the mean square spectral density of the output. Thus, the output spectrum is directly obtained from the input spectrum, via multiplication by the square of the RAO magnitude. Consequently, the RAO is formulated as follows:

$$RAO(\omega) = \sqrt{S_{yy}(\omega)/S_{xx}(\omega)} \tag{7}$$

where $S_{xx}(\omega)$ is input spectrum and $S_{yy}(\omega)$ is the output spectrum [64]. When the rotor is parked, RAOs show considerable excitation in the surge and pitch modes at the frequencies 0.011 Hz and 0.024 Hz, respectively (Figure 23). The effect of turbine rotation on RAO is also examined. In fact, it can be observed from Figures 23 that for operational condition an increase of the surge RAO by 162% at the surge natural frequency, whereas at the pitch natural frequency, the surge RAO is decreased by about 20%. It can be also highlighted the RAO peak at the heave natural frequency around 0.032 Hz under parked condition for both response surge and pitch, respectively. Furthermore, it is shown that influence of the rotation of the turbine blades increases the pitch RAO by 25% at the pitch natural frequency.

In general, pitch RAO at the pitch natural frequency has a lower value in rated conditions when compared with parked condition. On the contrary, surge RAO at the surge natural frequency is largely greater in rated condition than in parked condition. Furthermore, it is noted that RAO at low frequency part could be affected by the second-order wave loads effects.

For the two selected tests, results of the spectral analysis of surge and pitch motions are given in Figure 24. In particular, the response at the wave frequency around 0.1 Hz is clearly visible, together with the low frequency oscillations at the fundamental frequencies. It is noted that to operational condition gives a higher response in terms of surge and pitch natural oscillations. These results confirm the trends already observed through RAO. Furthermore, the 3X and 6X wave frequency peaks and the first elastic bending frequency at 1.6 Hz can be detected at the higher frequency range.

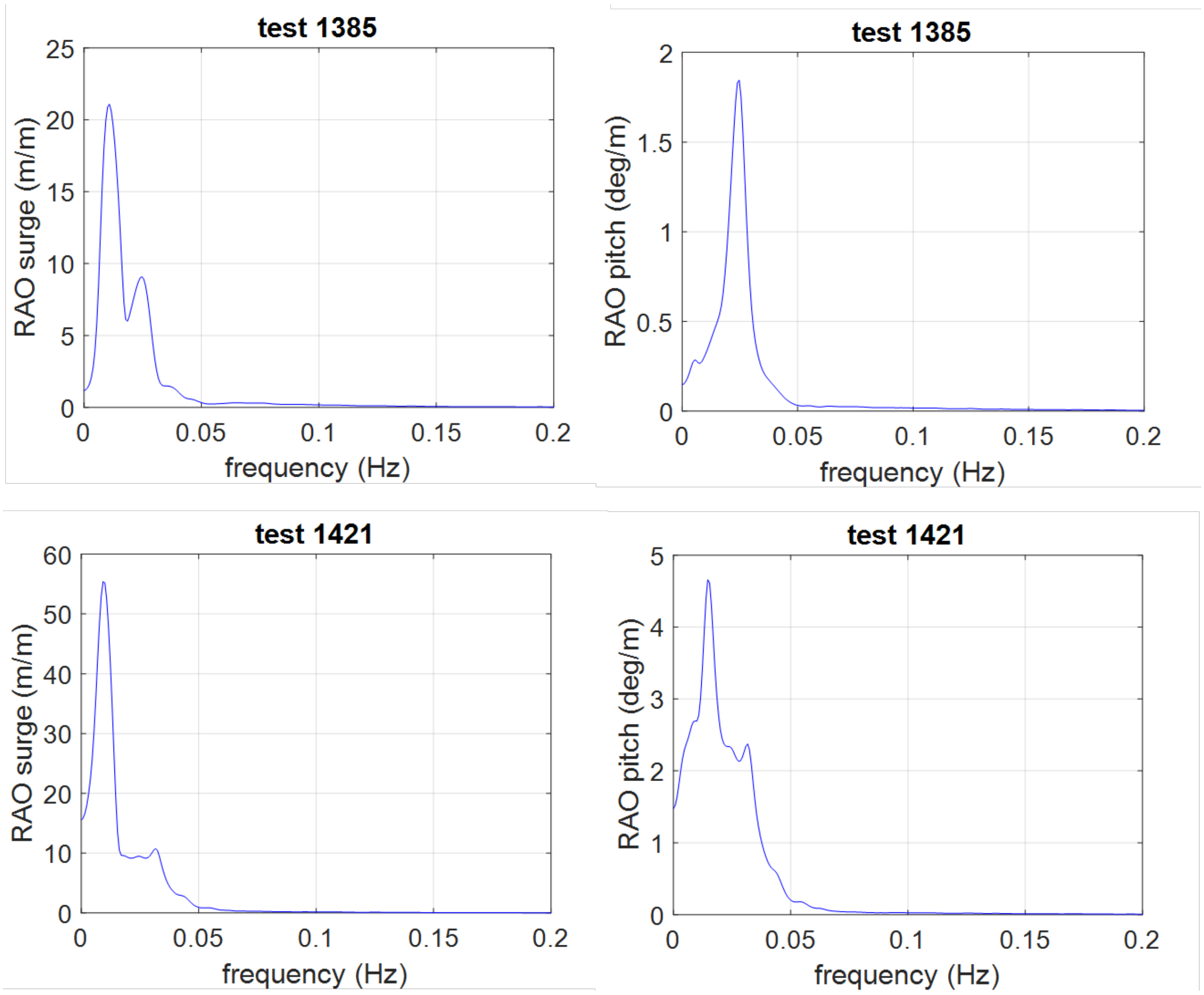

Figure 23. RAO surge (left) and pitch (right) for the selected irregular wave test generated by Hs=4m, parked condition (top) and operational condition (bottom).

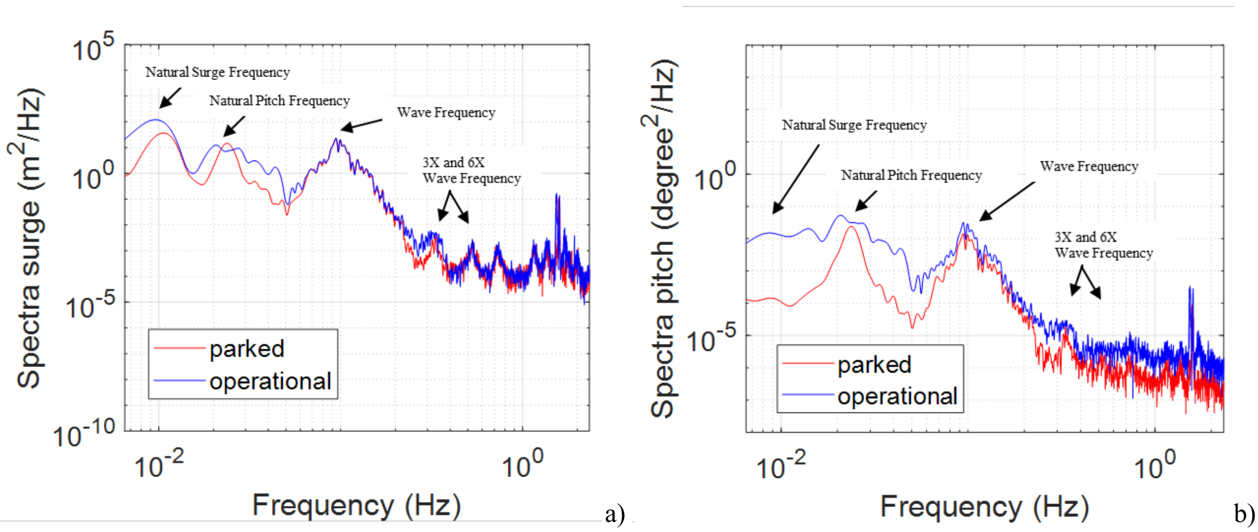

Figure 24. PSDFs of the surge (a) and pitch (b) under parked (red line) and operational (blue line) conditions.

The power corresponding to narrow ranges around the relevant frequencies, together with the total power of surge and pitch components measured in the experiments are given in Table 21. The wave frequency together with surge and pitch frequencies are always dominant, with contributions ranging from 96.4% to 99.2%.

Table 21. Surge and pitch narrow-band and total power (m^2).

	Surge		Pitch	
	Parked	Operational	Parked	Operational
Surge Frequency	9.67E-02	3.18E-01	4.71E-07	5.40E-05
Pitch Frequency	1.06E-01	2.27E-01	8.65E-05	5.87E-04
Wave Frequency	3.60E-01	3.85E-01	2.67E-04	5.90E-04
3X Wave Frequency	1.05E-04	2.29E-04	5.39E-07	1.65E-06
6X Wave Frequency	7.59E-05	8.88E-05	2.00E-07	6.65E-07
Total power	5.68E-01	9.50E-01	3.58E-04	1.28E-03

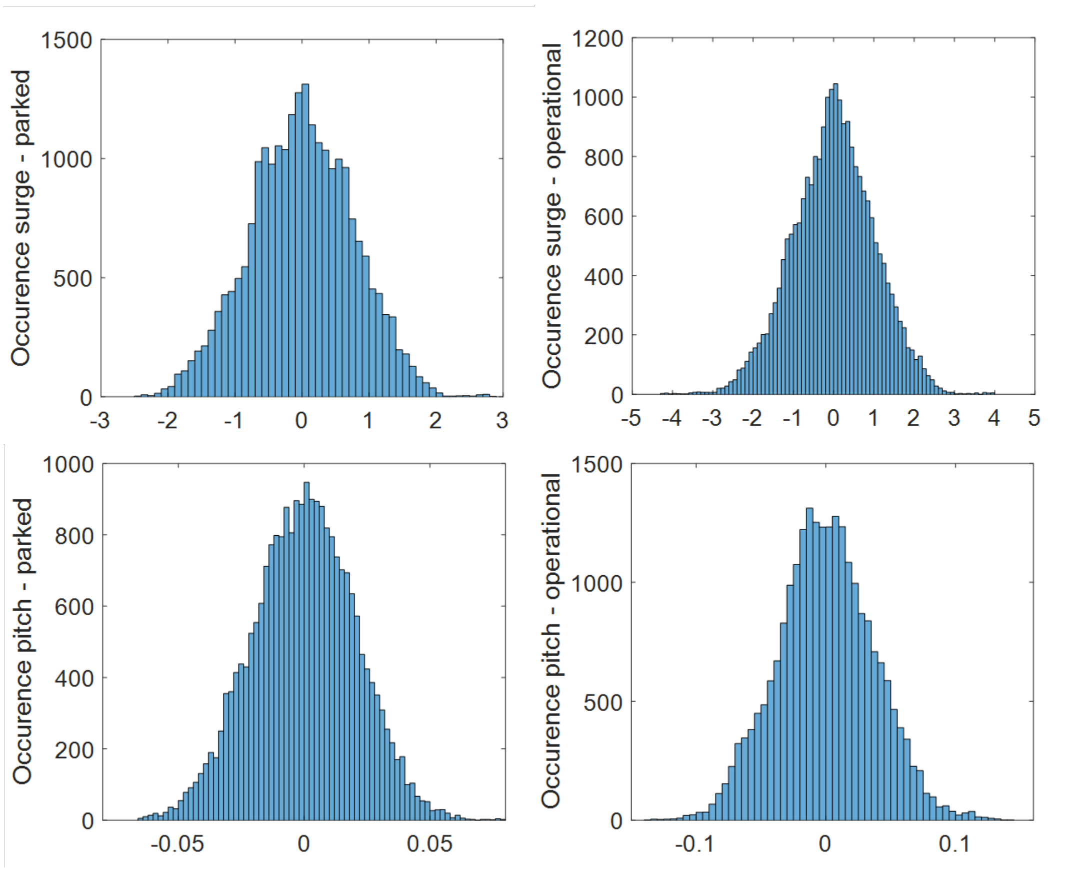

Figure 25. Histograms of the occurrence frequencies of surge (left) and pitch (right) as measured in tests under parked (top) and operational (bottom) conditions.

5.3.2 Peak factors and expected maxima

The presented results can be also used to evaluate the expected maxima of the response parameters. To this aim, the histogram of the occurrence frequencies of surge and pitch evaluated from tests #1385 and #1421 are shown in Figure 25. According to these diagrams, the surge and pitch motions appear to be well described by a narrowband process.

In Table 22, the STD of surge and pitch are summarized for the two tests. To the aim of obtaining expected response peak values, the peak factors were determined according to Vanmarcke. The peak factors, over a duration of 3,710 s (length of the tests), are also summarized in Table 22, together with the measured peak factors (in brackets) over the same record. It is observed that the prediction of the peak factor of the longitudinal components of the response is quite accurate, with average errors in the order of 2% in parked conditions and of 3% in operational conditions.

Table 22. STD and calculated (measured) peak factors of surge and pitch.

	STD		Peak Factors	
	Parked	Operational	Parked	Operational
H (m)	4		4	
Surge	0.7389	0.9727	3.68 (3.72)	3.72 (3.92)
Pitch	0.0189	0.0356	3.72 (3.86)	3.78 (3.83)

6. CONCLUSIONS

In the present paper, the feasibility of wave basin tests for investigating the dynamic response of a Spar Buoy Wind Turbine, has been investigated. Different regular and irregular wave heights have been considered, together with three different wind conditions. Displacements, accelerations, tower forces and mooring line forces have been measured and analysed.

First, free decay tests were carried out to detect the natural periods and the damping ratios. The measured full-scale rigid body oscillation frequencies were found to be 0.011 Hz in surge and sway and 0.024 Hz in pitch and roll. From measurement of the mooring line tensions in forced vibrations, also the heave frequency could be detected and found to be 0.034 Hz. The damping ratios coming from free decay test were compared with those measured in forced vibrations, showing a good agreement. In particular, values of 0.12%, 0.19%, 0.13% and 0.15% were found from free decay oscillations for surge, sway, roll and pitch, respectively when the fourth cycle of oscillation is considered. As a matter of comparison from forced vibration tests on the parked wind turbine a constant value of 0.12 was found for surge, and values in the range of 0.10 and 0.14 for operational conditions with a mean value of 0.12.

Analysis of the dynamic response in terms of displacements, accelerations and tower and mooring line forces reveals that this occurs mainly at the oncoming wave frequency, with smaller or larger components at its first and second harmonics. A component of the response was also found at the first elastic bending frequency of the tower; this, however, was not properly scaled, as the Cauchy number was not considered in the design of the model.

In particular, for the parameters associated with the longitudinal response in all tests the response is dominated by the wave frequency. It is noticed that in parked conditions the response increases with wave height at all frequencies of interest, whereas in operational conditions this trend is not always confirmed; this suggests that the gyroscopic effects and the rotor dynamics can somehow affect response. On the other hand, for the parameters associated with the lateral response the wave frequency is not always dominant and also the other harmonics are excited.

The comparison between the measured displacements and the corresponding tower forces highlights as the RMS of the surge is a meaningful measure of the dynamic response, being the measured forces in general monotonically increasing with it. This happens in particular for the longitudinal forces, which are clearly associated with the longitudinal inertia; however, for the lateral forces, the trend is still reasonably good.

Finally, peak factors were calculated using the bimodal methods for the longitudinal response components and using the Vanmarcke method for the lateral response components. The first proved to be rather accurate, whereas the second is more or less accurate depending on the parameter under investigation and on the rotor condition; this due to the more or less Gaussian nature of the process.

It can be concluded that wave basin tests are a useful tool for investigating the dynamic response of Spar Buoy Wind Turbine, provided that both Froude and Cauchy scaling are taken into account.

ACKNOWLEDGEMENTS

The present research has been supported by the EU Seventh Framework Programme (FP7) through the grant to the budget of the Integrated Infrastructure Initiative HYDRALAB IV (Contract Number: 261520) within the Transnational Access Activities.

REFERENCES

[1] C. Iuppa, L. Cavallaro, D. Vicinanza, E. Foti, Investigation of suitable sites for wave energy converters around Sicily (Italy), Ocean Science, ISSN 1812-0784, vol. 11 (2015) pp. 543-557, www.ocean-sci.net/11/543/2015/; http://dx.doi.org/10.5194/os-11-543-2015.

[2] P. Contestabile, D. Vicinanza, V. Ferrante, Wave Energy Resource along the Coast of Santa Catarina (Brazil), Energies, ISSN 1996-1073, vol. 8, (2015) Issue 12, 14219-14243. http://dx.doi.org/10.3390/en81212423.

[3] A. Uihlein and D. Magagna, Wave and tidal current energy – A review of the current state of research beyond technology, Renewable and Sustainable Energy Reviews, Volume 58, May (2016), Pages 1070-1081.

[4] T. Soukissian, F. Karathanasi, P. Axaopoulos, Satellite-Based Offshore Wind Resource Assessment in the Mediterranean Sea, IEEE Journal of Oceanic Engineering, vol. 42, (2017) no. 1, pp.73–86.

[5] P.C. Vicente, A.F. de O. Falcão, L.M.C. Gato, P.A.P. Justino, Dynamics of arrays of floating point-absorber wave energy converters with inter-body and bottom slack-mooring connections, Applied Ocean Research, 31 (4), (2009) pp. 267-281, DOI: 10.1016/j.apor.2009.09.002.

[6] D. Vicinanza, J.H. Nørgaard, P. Contestabile, T.L. Andersen, Wave loadings acting on overtopping breakwater for energy conversion. Journal of Coastal Research, Issue 65, (2013) pp. 1669-1674.

[7] M. Buccino, D. Stagonas, D. Vicinanza, Development of composite sea wall wave energy converter system. Renewable Energy, Issue 81, (2015) pp. 509-522.

[8] Stewart G., Muskulus M., A Review and Comparison of Floating Offshore Wind Turbine Model Experiments, Energy Procedia 94 (2016) 227-231, DOI: 10.1016/j.egypro.2016.09.228.

[9] P. Contestabile, E. Di Lauro, M. Buccino, D. Vicinanza, Economic assessment of Overtopping BReakwater for Energy Conversion (OBREC): a case study in Western Australia, Sustainability, ISSN 2071-1050, 9(51); (2017) http://dx.doi.org/10.3390/su9010051.

[10] E. Segura, R. Morales, J.A. Somolinos, A strategic analysis of tidal current energy conversion systems in the European Union (Review), Applied Energy, Volume 212, 15, (2018) Pages 527-551.

[11] W. E. Heronemus, Pollution-free energy from offshore winds, 8th Annual Conference and Exposition Marine Technology Society, Washington D.C., September 11-13, 1972.

[12] S. Butterfield, W. Musial, J. Jonkman, P. Sclavounos, Engineering challenges for floating off-shore wind turbines, Technical Report NREL/TP-500-38776 (2007).

[13] B.M. Sumer, J. Fredsoe, Hydrodynamics around cylindrical structures, Advanced Series on Coastal Engineering, 12, World Scientific, Singapore (2006).

[14] F. Aristodemo, G.R. Tomasicchio, P. Veltri, New model to determine forces at on-bottom slender pipelines. Coastal Engineering 58 (2011), pp. 267-280.

[15] J. Jonkman, D. Matha, A quantitative comparison of the responses of three floating platforms. Proceedings of European Offshore Wind 2009 Conference and Exhibition, NREL/CP-500-46726 (2009).

[16] G. Salvadori, F. Durante, G.R. Tomasicchio, F. D'Alessandro, Practical guidelines for the multivariate assessment of the structural risk in coastal and off-shore engineering, Coastal Engineering 95 (2015), pp. 77-83.

[17] G. Salvadori, G.R. Tomasicchio, F. D'Alessandro, Multivariate approach to design coastal and off-shore engineering, Journal of Coastal Research Special Issue (65) 1, (2013), pp. 386-391.

[18] G. Salvadori, G.R. Tomasicchio, F. D'Alessandro, Practical guidelines for multivariate analysis and design in coastal engineering, Coastal Engineering 88 (2014), pp. 1-14.

[19] C.H. Lee, WAMIT Theory Manual, MIT Report 95-2, Dept. of Ocean Eng., MIT (1995).

[20] C.H. Lee, Wave interaction with huge floating structure, BOSS'97, Delft, The Netherlands (1997).

[21] J. N. Newman, P. D. Sclavounos, The computation of wave loads on large offshore structures, Proceedings 5th International Conference on the Behaviour of Offshore Structures BOSS `88 Trondheim, Norway (1988).

[22] P. Ghadimi, H.P. Bandari, A.B. Rostami, Determination of the heave and pitch motions of a floating cylinder by analytical solution of its diffraction problem and examination of the effects of geometric parameters on its dynamics in regular waves. International Journal of Applied Mathematical Research, 1(4), (2012), pp. 611-633.

[23] L. Wan, Z. Gao, T. Moan, Experimental and numerical study of hydrodynamic responses of a combined wind and wave energy converter concept in survival modes, Coastal Engineering 104 (2015), pp. 151-169.

[24] A. Jain, A.N. Robertson, J.M. Jonkman, A.J. Goupee, R.W. Kimball, A.H.P. Swift, FAST Code Verification of Scaling Laws for DeepCwind Floating Wind System Tests, 22nd Int. Offshore and Polar Eng. Conf. Rhodes, Greece, June 17–22 (2012).

[25] R.A. Smith, W.T. Moon, W.T. Kao, Experiments on flow about a yawed circular cylinder, ASME Paper N. 72-FE-2 (1972).

[26] M.B. Bryndum, D.T. Tsahalis, V. Jacobsen, Hydrodynamic forces on pipelines: model tests, J. of Offshore Mechanics and Arctic Engineering 114(4), (1992), pp. 231-241.

[27] B. Brunone, G.R. Tomasicchio, Wave kinematics at steep slopes: second-order model, Journal of Waterway, Port, Coastal and Ocean Engineering 123-5, (1997), pp. 223-232.

[28] P. Lomonaco, R. Guanche, C. Vidal, I.J. Losada, L. Migoya, Measuring and modelling the behaviour of floating slender bodies under wind and wave action, Proc. Int. Conf. Coastlab 10, Barcelona, 54 (2010).

[29] F.G. Nielsen, T.D. Hanson, B. Skaare, Integrated dynamic analysis of floating offshore wind turbine. Proc. Int. Conf. on Ocean, Offshore and Arctic Engineering, Am. Soc. Mech. Eng. (ASME), New York (2006).

[30] B. Skaare, T.D. Hanson, F.G. Nielsen, R. Yttervik, A.M. Hansen, K. Thomsen, T.J. Larsen, Integrated dynamic analysis of floating offshore wind turbines. In Proceedings of the European Wind Energy Conference & Exhibition (EWEC), Milan, Italy, 7–10 May (2007).

[31] B. Skaare, Development of the Hywind concept, Proceedings of the ASME 36th International Conference on Ocean, Offshore and Arctic Engineering, OMAE2017-62710, June 25-30, Trondheim, Norway (2017).

[32] T. Utsunomiya, T. Sato, H. Matsukuma, K. Yago, Experimental validation for motion of a spar- type floating offshore wind turbine using 1/22.5 scale model, Proc. Int. Conf. on Ocean Offshore and Arctic Engineering, Am. Soc. of Mech. Eng. (ASME), New York (2009).

[33] H. Shin, Model test of the OC3-Hywind floating offshore wind turbine, Proceedings of 21st ISOPE. Maui, Hawaii, USA June 19-24 (2011).

[34] A. Myhr, K.J. Maus, T.A. Nygaard, Experimental and computational comparisons of the OC3-Hywind and tension-leg-buoy (TLB) floating wind turbine conceptual designs. In Proceedings of the International Society of Offshore and Polar Engineering Conference, Hawaii, HI, USA, 19–24 June (2011).

[35] H.R. Martin, R.W. Kimball, A.M. Viselli, A.J. Goupee, Methodology for Wind/Wave Basing Testing of Floating Offshore Wind Turbines Proceedings of the 31st International Conference on Ocean, Offshore and Arctic Engineering Rio de Janeiro, Brazil June 10-15 (2012).

[36] A.J. Goupee, B.J. Koo, R.W. Kimball, K.F. Lambrakos, H.J. Dagher, Experimental Comparison of Three Floating Wind Turbine Concepts, J Offshore Mech Arct Eng, 136(2), 021903, (2014).

[37] B.J. Koo, A.J. Goupee, K.W. Kimball, K.F. Lambrakos, Model Tests for a Floating Wind Turbine on Three Different Floaters, J Offshore Mech Arct Eng, 136(2), 021904 (2014).

[38] L. Sethuraman, V. Venugopal, Hydrodynamic response of a stepped-spar floating wind turbine: Numerical modeling and tank testing, Renew. Energy, 52, 160–174 (2013).

[39] S. Nallayarasu, S. Saravanapriya, Experimental and numerical investigation on hydrodynamic response of spar with wind turbine under regular waves (Part I), International journal of ocean and climate systems, Multi-Science Publications, UK., Vol. 4, Issue 4, pp. 239-260 (2013).

[40] S. Nallayarasu, S. Saravanapriya, Experimental and numerical investigation on hydrodynamic response of spar with wind turbine under random waves (Part II), International journal of ocean and climate systems, Multi-Science Publications, UK., Vol. 3, pp.261-282 (2013).

[41] C. Ruzzo, V. Fiamma, V. Nava, M. Collu, G. Failla, F. Arena, Progress on the experimental set-up for the testing of a floating offshore wind turbine scaled model in a field site, Wind Engineering, 40 (5), 455-467 (2016).

[42] G.R. Tomasicchio, A.M. Avossa, L. Riefolo, F. Ricciardelli, E. Musci, F. D'Alessandro, D. Vicinanza, Dynamic modelling of a spar buoy wind turbine, Proc. 36th Int. Conf. on Ocean, Offshore and Arctic Engineering, Am. Soc. of Mech. Eng. (ASME), Trondheim, Norway (2017).

[43] S. Butterfield, W. Musial, J. Jonkman, P. Sclavounos, Engineering challenges for floating wind Turbines. Re-port number NREL/CP-500-38776. Colorado: National Renewable Energy Laboratory NREL (2007).

[44] J. Jonkman, Definition of the floating system for phase IV of OC3, report number NREL/TP-500-47535. Colorado: National Renewable Energy Laboratory NREL (2010).

[45] J. Jensen, A. Olsen, A. Mansour, Extreme wave and wind response predictions. Ocean Engineering, 38(17-18), pp.2244-2253 (2011).

[46] L. Wang, B. Sweetman, Simulation of large –amplitude motion of floating wind turbines using conservation of momentum. Ocean Engineering, 42, pp.155-164 (2012).

[47] H. Shin, S. Cho, K. Jung, Model test of an inverted conical cylinder floating offshore wind turbine moored by a spring-tensioned-leg. International Journal of Naval Architecture and Ocean Engineering, 6(1), pp.1-13 (2014).

[48] J. Jonkman, Dynamics of offshore floating wind turbines-model development and verification. Wind Energy, 12, pp.459-492 (2009).

[49] M. Karimirad, Q. Meissonnier, Z. Gao, T. Moan, Hydro elastic code-to-code comparison for a tension leg SPAR-type floating wind turbine. Marine Structures, 24(4), pp.412-435 (2011).

[50] A.A. Dodaran, S.K. Park, Development of design static property analysis of mooring system caisson for off-shore floating wind turbine. International Journal of Ocean System Engineering, 2(2), pp.97-105 (2012).

[51] J. Jonkman, W. Musial, Offshore code comparison collaboration (OC3) for IEA task 23 offshore wind technology and development, report number NREL/TP-5000-48191. Colorado: National Renewable Energy Laboratory NREL (2010).

[52] O.M. Faltinsen, Sea loads on ships and offshore structures, Cambridge University Press (1990).

[53] S.A. Mavrakos, STATMOOR User’s manual, Laboratory for Floating Stuctures and Mooring Systems, School of Naval Architecture and Marine Engineering, National Technical University of Athens (1992).

[54] P.D. Sclavounos, C. Tracy, S. Lee, Floating off-shore wind turbines: responses in a sea state, Pareto optimal designs and economic assessment, Proc. 27th Int. Conf. on Off-shore mechanics and arctic engineering, OMAE (2008).

[55] E.P.D. Mansard, E.R. Funke, The measurement of incident and reflected spectra using a least squares method. Proc. 17th Int. Conf. on Coastal Engineering, Sidney, Australia (1980), pp. 154-172.

[56] IEC 61400-1, Ed. 2, Wind Turbine Generator Systems, Part 1: Safety Requirements (1999).

[57] IEC 61400-3, Ed1, Wind turbines, Part 3: Design requirements for offshore wind turbines (2009). alifornia at Berkeley, Fourth Edition, Prentice Hall (2012).

[58] M. Karimirad, Offshore Energy Structures For Wind Power, Wave Energy and Hybrid Marine Platforms, Springer (2014).

[59] J.R. Browning, J. Jonkman, A. Robertson, A.J. Goupee, Calibration and validation of a spar-type floating offshore wind turbine model using the FAST dynamic simulation tool, Journal of Physics: Conference Series 555 (2014) 012015.

[60] E.H. Vanmarcke, On the distribution of the first-passage time for normal stationary random processes, J. Appl. Mech. 42 (1975), p.215-220.

[61] A.G. Davenport, Note on the distribution of the largest value of a random function with application to gust loading, Proc. Inst. Civ. Eng. (1964), pp. 187–196.

[62] C. Braccesi, F. Cianetti, G. Lori, D. Pioli, A Frequency Method for Fatigue Life Estimation of Mechanical Components under Bimodal Random Stress Process, SDHM Structural Durability and Health Monitoring 1-4 (2005), pp. 277-290.

[63] P. Folgueras, S. Solari, M. Mier-Torrecilla, M. Doblaré, M.A. Losada, The extended Davenport peak factor as an extreme-value estimation method for linear combinations of correlated non-Gaussian random variables, J. Wind Eng. Ind. Aerodyn. 157 (2016), pp. 125–139.

[64] E.M. Lewandowski, The dynamics of marine craft, Maneuvering and Seakeeping, Advanced Series on Ocean Engineering - Volume 22. (2004).